RESEARCH ARTICLE

WILEY

Advanced multimaterial shape optimization methods as applied to advanced manufacturing of wind turbine generators

Latha Sethuraman[1] | Andrew Glaws[2] | Miles Skinner[1] | M. Parans Paranthaman[3]

[1]National Wind Technology Center, National Renewable Energy Laboratory, Golden, Colorado, USA

[2]Computational Science Center, National Renewable Energy Laboratory, Golden, Colorado, USA

[3]Chemical Sciences Division, Oak Ridge National Laboratory, Oak Ridge, Tennessee, USA

Correspondence
Latha Sethuraman, National Wind Technology Center, National Renewable Energy Laboratory, Golden, CO, USA.
Email: Latha.Sethuraman@nrel.gov

Funding information
Wind Energy Technologies Office

Abstract

Currently, many utility-scale wind turbine generator original equipment manufacturers are dependent on imported rare earth permanent magnets, which are susceptible to market risks from cost instability. To lower the production costs of these generators and stay competitive in the market, several small wind manufacturers are pursuing continuous improvements to both generator design and manufacturing. However, traditional design and manufacturing methods have yielded marginal improvements in wind power performance. This work presents novel methods to redesign a baseline 15-kW wind turbine generator with reduced rare-earth permanent magnets by leveraging cutting-edge three-dimensional (3D) printed polymer-bonded permanent magnets and steel. Symmetric, asymmetric, and multimaterial-magnet parametrization methods are introduced for shape optimization. We extend the symmetric and asymmetric methods to the back iron in the stator to further investigate the impact and opportunities for performance improvements with lesser active materials. We employ a design-of-experiments approach with parametric computer-aided design for shape generation and evaluate different designs by magneto-thermal modeling and finite-element analysis. We use adaptive sampling technique to identify better performing designs with lesser magnet mass, higher efficiency, and lower cogging torque when compared with the baseline generator. Asymmetric pole designs resulted in a magnet mass in the range of 4.77–5.37 kg, which was 27%–35% lighter than the baseline generator, suggesting that a new design freedom exists that can be enabled by advanced manufacturing, such as 3D printing. Shaping the back iron in the stator resulted in material savings in electrical steel of up to 14.62 kg, which was 20% lighter than the baseline stator. We conducted a structural analysis to evaluate an optimized asymmetric rotor design from the point of view of mechanical integrity and air-gap stiffness. The magnetically optimal shape profile was shown as having a positive impact on the radial stiffness, and an optimal solution was discovered to reduce the structural mass by nearly 30 kg, which was 29% lighter than the baseline.

KEYWORDS
3D printed magnets, adaptive sampling, Bézier curves, parametrization, structural analysis

1 | INTRODUCTION

Direct-drive permanent-magnet synchronous generators (DDPMSGs) are a popular choice in several small wind turbines installed in the United States.[1,2] As the costs of installing these small wind turbines continue to rise,[3] many of the original equipment manufacturers of these small wind turbines are pursuing measures to improve the cost competitiveness and generator performance in terms of efficiency and reliability. A certain portion of costs in these generators comes from permanent magnets that are impacted by price uncertainties and an unstable supply chain.[4] The availability of other key raw materials such as cold-rolled electrical steel is also experiencing price increases of more than 400%. These increases are greatly limiting the ability of many original equipment manufacturers (OEMs) to produce machines at lower costs.[5] Although DDPMSGs are advantageous in terms of noise elimination and low maintenance, their manufacturing costs alone can be as high as 60% of the turbine costs.[6] Thus, small-wind generator OEMs are constantly pursuing innovations in generator manufacturing, design, and materials to achieve economies at scale.

In terms of improving generator performance, researchers have attempted increasing the efficiency of power generation and lowering the cogging torque in these machines. For instance, Muljadi and Green[7] observed improved cogging torque profiles by using nonuniform poles (e.g., bread loaf magnets), by skewing poles and by varying the pole arc to pole pitch ratio. However, each of these techniques tends to increase tooling and manufacturing costs. Improvements in generator efficiency have been made possible by using concentrated windings and altering slot and tooth geometry to reduce eddy current losses in magnets and stator laminations. Such laminations are typically manufactured by multistage forming processes that limit the minimal achievable thickness to 0.2–0.65 mm.[8] As a result, the ohmic power loss by eddy current losses in the core and magnets can be significant, and the heat produced in a solid rotor yoke can cause irreversible demagnetization. Conventional lamination fabrication generates significant material waste, potentially exceeding 50% due to scrap generation during cutting and punching processes. On the other hand, machining of sintered magnets and casting steel to required geometric tolerances require expensive tooling and molds. Conventionally sintered magnets are produced in simple geometrical forms like rectangular bars or arc-shaped magnets. Because of the high level of hardness and brittleness, postsinter machining of the sintered magnets to produce more complex-shaped magnets is greatly limited, thereby limiting the full design freedom.

Traditional design approaches for wind turbine generators leverage such standard geometries defined using arcs and line segments owing to their well-established performance. Simple geometries can also help minimize eddy current losses and magnetic saturation and are easier to fabricate using machining and stamping. Designers have often used simple geometries, such as the arc shape in magnets, because of their reliability and familiarity. Some of these shapes have also become standardized because of their proven performance, leading to economies of scale. Numerical modeling tools can also easily handle simple geometries, thereby allowing engineers to perform simulations that can predict the performance under different operating conditions. However, modern approaches that leverage advanced manufacturing techniques and computational tools are emerging that can help overome several performance limitations.

1.1 | Recent developments in manufacturing and design of electric machines

Notable progress has been made in near-net shaping techniques and manufacturing for electrical steel and magnets, allowing for highly intricate profiles that were previously impossible to manufacture using traditional methods.

1.1.1 | Electrical steel manufacturing

High-precision laser cutting[9] and micromachining systems are increasingly used for precise shaping of electrical steel lamination when high cutting accuracy is needed. Because they are flexible to design changes without the need for retooling, the systems are beneficial for parts manufactured with multiple materials or different material thicknesses and can help minimize material offcuts that occur when forming. Another emerging technology called photochemical etching[10] involves selectively removing material from a piece of sheet metal using an etchant, which is exposed to a pattern of light that prints the design onto the sheet. This causes some areas to soften and facilitate easy removal without contact; it also preserves the magnetic properties. Sheet hydroforming is also gaining popularity wherein a high-pressure hydraulic fluid is employed to shape metals using a single mold. Benefits of this method include reducing material wastage by up to 70% and creating lighter, stronger parts with complex shapes and high dimensional accuracy.[11] Additive manufacturing techniques are also being researched to enable complex geometries in electric machines. Electrical steel with higher silicon content has been demonstrated using binder jet additive manufacturing methods.[12] Stator laminations with 3% silicon content have been successfully printed using selective laser melting (SLM), followed by wire-cut electric discharge machining (EDM) to thin laminates, and stacking.[13] More recently, Oak Ridge National Laboratory (ORNL) is exploring multimaterial printing by incorporating aluminum alloys into electrical steel during printing followed by annealing.[14] This process could eliminate the need for EDM slicing. Large-format sand mold printers are also emerging[15,16] and offer the potential to enable complex shaped castings up to 9.5 m in diameter and 60-plus t in

weight. It is therefore possible to leverage these technologies to print the mold of a complex-shaped electrical steel core and cast the molten metal.

1.1.2 | Magnet manufacturing

To date, magnet shaping has been possible with polymer-bonded magnets manufactured by injection or compression molding. In terms of binder-free magnets, a waste-free approach to the net-shape production of anisotropic Nd-Fe-B magnets is shown possible by pulsed-current-activated, pressure-assisted sintering or spark-plasma sintering.[17] A popular material extrusion technique, namely, fused deposition modeling (FDM), has been used to fabricate bonded magnets that have been shown to be superior to commercial-grade polymer-bonded magnets and offer multiple advantages.[18] These advantages include increasing magnet supply chain by allowing for recyclability and the absence of molds that can significantly lower the manufacturing costs when compared with injection-molded magnets. More recently, 81-vol%-printed polymer-bonded magnets were obtained from composite pellets made from a starting magnet powder–Magfine MF15P[19]–using the Big Area Additive Manufacturing system[20] and an iterative process that progressed from 70–75 vol%. MF15P are a series of heat-resistant powders made from Nd-Fe-B+Sm-Fe-N +Nylon 12 that do not contain dysprosium and have an energy product of 38 MGOe. To achieve an optimum combination of remanence and coercivity with printed magnets, the authors optimized the ratios of the coarse NdFeB powder and fine SmFeN powder, the content of the binder, and the processing conditions. Figure 1 (adapted from[21]) shows a comparison of the demagnetization curves for the sintered magnet, 75-vol %-printed polymer-bonded magnets, and commercial injection-molded magnet that was manufactured using such powder and Nylon 12. The demagnetization properties for 75-vol%-printed magnets were linearly extrapolated from measurements on 70-vol%-printed magnets. The measurements were made using a vibrating sample magnetometer and were used for generating the hysteresis loop of the printed magnets at various temperatures from 300–400 K. Table 1 presents a comparison of magnetic, electrical, and mechanical characteristics of all three magnet types.
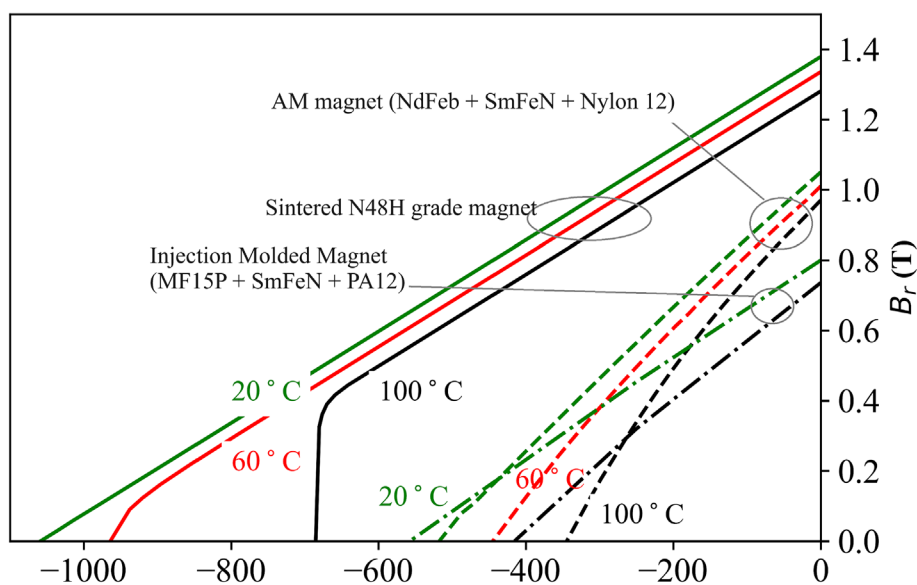
FIGURE 1 A comparison of demagnetization curves (black, red, and green lines represent properties at 100°C, 60°C, and 20°C, respectively.

TABLE 1 Comparison of magnet properties.

Property	N48H NdFeB[21]	AM 75 vol% MF15P-SmFeN+PA12[21]	Injection MF15P-SmFeN+PA12[19]
Remanence, B_r(T)	1.36	1.03	0.89
Intrinsic covercivity, $_iH_c$ (kA/m)	1041.7	684.2	954.93
Energy product, BH_{max} (MGOe)	45	20	17.5
Density, ρ_{mag} (kg/m^3)	7600	6150	5400
Temperature coefficient of H_c (%/deg.C)	−0.58	−0.61	−0.46
Electrical resistivity ($\Omega \cdot$ m)	150E-4	0.170	0.1−0.2

Note that the printed magnet has a higher remanence and lower coercivity when compared to the magnet manufactured by injection molding. Further, both of these methods suggest no clear knee point, with the possibility of occurrence in the third quadrant. From an electric machine's design point of view, the combination of high remanence and coercivity would be essential to enable high air-gap torque without loss in performance at high temperatures. Although polymer-bonded magnets have a lower coercivity, near-linear demagnetization characteristics and high electrical resistivity would allow the machine and magnets to operate with lower magnetization with better thermal stability up to 450 K[22] without the risk observed with sintered magnets. Also, the polymer binder provides superior resistance to eddy currents and corrosion and allows pressing of the magnet onto the rotor core using an *insert molding* technique[23] without using special adhesives for bonding. Printed magnets also have tensile strength in the range of 32–52 MPa, which provides the needed stiffness against the centrifugal forces acting in low-speed machines. Few recent studies have leveraged some of these new methods for manufacturing and materials for electrical steel and magnets to improve the performance of conventional radial flux PMSGs using advanced design optimization approaches.
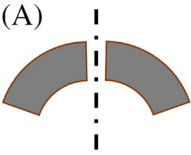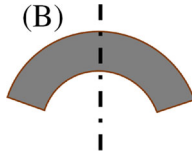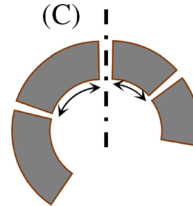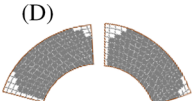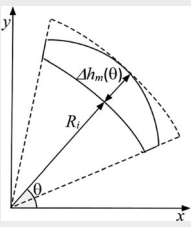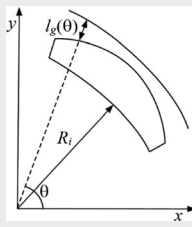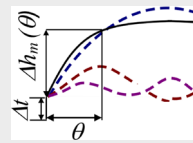
1.1.3 | Advanced design optimization for realizing complex geometries

Magnet geometries have been altered using *Topology optimization* methods by accurately controlling the material placement within a Cartesian mesh with element-wise variation of material density.[24,25] Level set approaches requiring no geometric parametrization have also been used.[26] Both techniques have demonstrated improvements to torque density with less rare earth material. However, because the optimization is generally not conditioned with manufacturing constraints, checkered patterns or sharp corners may result, which can increase saturation from magnetic field concentrations as well as stress concentrations.

Electrical steel geometries have been altered using *shape optimization* techniques that alter the bounding lines and arc using boundary points that serve as design variables. Parametric curves, such as B-splines,[27,28] have been used for rotor shaping in small motors to minimize vibration and harmonic distortion in back-electromotive force waveforms. The methods are usually followed by shape-sensitivity analysis requiring advanced techniques for derivation. Sethuraman and Vijayakumar[29] used Bézier curves to optimize the rotor of a 15-MW generator using a parametric computer-aided design (CAD) tool. The study used a design of experiments (DoE) approach that allowed for quicker evaluation of shape sensitivity and the realization of unique curvatures that deviated from the traditional arcs that can be fabricated by three-dimensional printing.

Radial pole-shaping methods have been used; however, considerable effort has been spent by others in finding a suitable shaping method. Common shape optimization methods for radially magnetized poles use sine, inverse cosine (Table 2), and eccentric optimization.[30] Both sine and inverse cosine shaping optimize the thickness of the permanent magnet. While sinusoidal shaping directly alters the thickness of the magnet (δh_m), inverse cosine shaping alters magnet shape indirectly by varying the air-gap length (l_g) according to a function of the rotor position angle (θ). As an extension of these shaping techniques, higher order harmonics (e.g, fifth harmonic or seventh harmonic) are also injected to achieve more

TABLE 2 Magnet pole-shaping techniques: (a) similar widths, (b) magnet with a similar shape about an axis, (c) magnets with a dissimilar pole arc, and (d) topology-optimized poles.

Symmetry Type		Asymmetry Type	
(A)	(B)	(C)	(D)
Intrapolar symmetry	Symmetric profile	Intrapolar asymmetry	Asymmetric profiling
Shaping approach			
Sine	Inverse cosine	Injecting higher harmonics	Grid-based

$$\Delta h_m(\theta) = \Delta m \left(\Sigma a_p \sin(p\theta) \right)$$

complex shapes that can improve average torque.[31] With sintered magnets having lower temperature resistance, this profiling is known to increase the risk of demagnetization, especially on the thinner, more vulnerable sides of the magnets.[32] Further, these approaches have mostly focused on shaping the magnets on the side closer to the air gap, whereas shaping the rear side of the magnet has never been attempted. Pole shaping is also combined with varying positions of the magnets within pole pitch to minimize ripple and cogging torque[33,34] or sensorless control. Pole shaping using grid-based topology optimization techniques increases complexity in design and modeling,[35] and the poles are difficult to manufacture.

1.1.4 | Symmetrical and asymmetrical designs

Most published literature on optimization of PMSGs is classified under symmetrical design approach, which assumes that a given geometry has identical distribution of materials about a geometric central axis. Consequently, the electromagnetic characteristics get repeated on every pole pair, which is an approach better suited for electric machines that need to rotate in both clock-wise and counter-clock-wise directions. This approach has been generally used to reduce complexity with geometry and performance parameters optimized to minimize the cost and time for high-volume production.[36] In contrast, limited research has been reported with asymmetrical design approaches.[33,35,37–40] Skewing is the most popular asymmetric design technique employed in PM machines for torque ripple production. However, minimum skewing stacks practically limit the implementation. Pole asymmetries have been implemented either using interpolar and intrapolar approaches.[38] Interpolar asymmetry corresponds to unequal distribution of materials within a pole, whereas intrapolar asymmetry refers to a case where adjacent poles of the machine are different. These techniques are attractive for optimizing PM machines that are exclusively intended for unidirectional operation.[39]

While industrial production of generators is presently limited to manufacture of symmetric designs, asymmetrical electric machine designs may not fit well within traditional manufacturing molds or tooling. The novel shaping techniques discussed earlier and 3D printing have the potential to eliminate these constraints by employing fabrication that relies on digital models. These techniques offer the advantage of adding material only where needed, thereby aligning with the weight-saving potential of asymmetrical electric machine designs. As large-scale metal printers are emerging, this opens up a new opportunity for realizing better-performing electric machines including asymmetric machine configurations that have been explored to some degree in the past, but to a much lesser extent for wind turbine generators.[37]

Because wind turbine generators operate in one direction for more than 95% of the time, they can be better designed for unidirectional operation using an asymmetrical approach that allows for each pole to have its own dimensional freedom and more optimal use of rare-earth material. Because asymmetry can change the inductance profile, it may also be possible to achieve a directionally dependent air-gap torque profile with improved performance in one specific rotation direction. Variable air-gap profiles can also be realized that can help lower total harmonic distortion in back-electromotive force waveforms.[33] Design for additive manufacturing can help explore specific asymmetric phenomena for performance improvements with reduced material usage.

1.2 | Article contributions

In this article, we leverage recent developments in magnet additive manufacturing to explore novel symmetric and asymmetric shapes for the electromagnetically active parts in a wind turbine generator. We used the Bézier-curve approach initially presented by Sethuraman and Vijayakumar[29] to initially perform multimaterial shape optimization of magnets and the rotor core[41] in a 15-kW DDPMSG used in a small wind turbine. Following up on the initial findings, we conducted a more in-depth analysis of the results by including a deeper assessment on performance sensitivity to magnet shapes, magnet thermal stability, and magnetic pressure loading in the air gap. We then extended the parametrization approach to optimize the stator core. We explored three approaches to geometric parametrization for shaping the rotor core and magnet regions. We then used the most optimal rotor design satisfying the performance criteria for a subsequent shaping of the stator core. We finally evaluated the structural integrity of a magnetically optimized rotor design by further exploring opportunities for the rotor for light-weight construction and maximum air-gap stiffness (i.e., radial stiffness). We adopted a decoupled multiphysics design approach with 3D-printed magnet materials to explore novel magnet geometries. These optimized geometries yielded target performance improvements in terms of efficiency and cogging torque reduction while also exhibiting reduced demagnetization risk with reduced rare earth materials. The article is organized as follows: Section 2 describes the baseline generator geometry and materials used for the optimization study. Details of model setup and analysis are presented in Section 2.2. Section 3 discusses the Bézier curve methodology for shape parametrization. Section 4 covers the design workflow with details on the sampling technique for generating the designs, shape sensitivity and methodology for structural analysis. The results of the analysis and conclusions are presented in Sections 5 and 6.

2 | BASELINE DESIGN SPECIFICATIONS OF THE GENERATOR AND MATERIALS

The baseline DDPMSG is an outer-rotor, radial-flux machine with 50 surface-mounted magnets. The design uses a double-layer concentrated winding with 60 slots (See Figure 2 for one periodicity). The generator is designed to deliver a rated power of 15 kW at 150 rpm in a wind speed of 11 m/s. For simplifying the analysis, the generator is assumed to be connected to the grid via a three-phase, back-to-back full-rated power converter and relies on an electromagnetic braking system during stalling, which uses a system whose details are described in Labuschagne et al.[21]

The minimum stall power during extreme weather events was taken as 40 kW. The machine outer diameter is about 635 mm (25 inches), and the axial stack length is about 150 mm (5.9 inches). The baseline machine utilizes custom-fabricated arc-shaped (solid pole) magnets of N48H-grade NdFeB material that are radially magnetized. They are adhered to a cylindrical rotor made of AISI 1020 low carbon steel. The stator core incorporates ASTM A677 standard M-15-grade electrical steel laminations and the windings have an H-grade insulation. Based on the assumption that a rapid fault clearing mechanism will prevent sustained overcurrents during faults, the maximum magnet allowable operating temperature was limited to 60°C.

2.1 | Magnet materials for printable designs

The mechanical and electromagnetic properties for magnets used in this design optimization study correspond to an innovative composite magnet made of 75-vol% NdFeB-SmFeN-Nylon that was fabricated using the BAAM system at ORNL. Figure 1[21] shows the normal B-H curves that were used to model these magnets. Considering the large dimensions of the machine, the rotor core was assumed to be fabricated by sand printing of a core mold followed by casting. This was a reasonable assumption to make because commercially available sand printers allowed for parts as large as 1 m by 1 m by 1 m to be fabricated by indirect additive manufacturing without altering the physical properties of the metal part. We propose to print the mold of the optimized rotor core and then cast wrought carbon B-grade steel (e.g., A216-grade steel). This way, the properties are comparable with AISI 1020 low carbon steel. Once the rotor core is fabricated, the shape-optimized magnets can be printed and attached to the
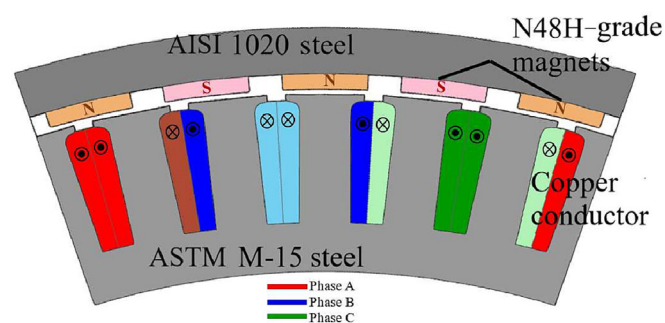
FIGURE 2 Permanent-magnet generator design used in a 15-kW turbine (dark and light shades of red, blue, and green colors represent positive and negative orientations for current in the respective phase conductors).
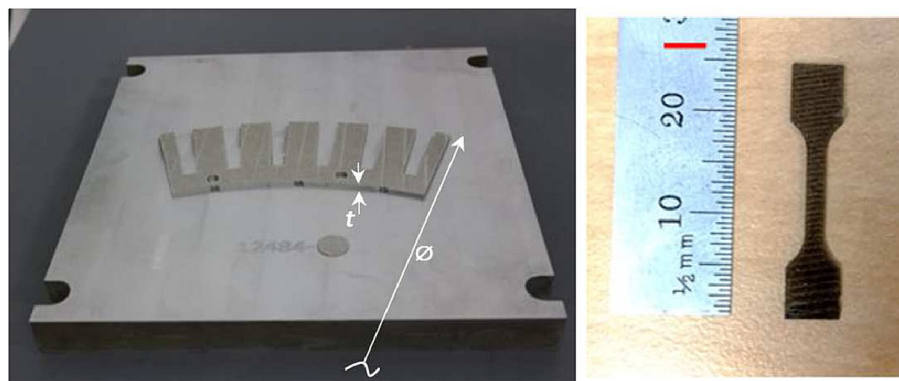
FIGURE 3 Printed stator laminate. Left: single laminate of $1/10^{th}$ sector of the 15-kW machine. Dimensions include the diameter, $\oslash = 21.6$" and thickness, $t = 0.020$". Right: dog-bone specimen of the same sample used for electrical and mechanical property measurements.

rotor core by insert-molding as described previously. The stator electrical steel laminations assumed properties for a sector fabricated by SLM (Figure 3). The rotor core is functionally both magnetic and structural; therefore, the optimization was first focused on minimizing the magnetic materials and then on verifying structural integrity. The properties of printed electrical steel are listed in Table 3.

2.2 | Magnetic and thermal finite-element analysis (FEA) models

A two-dimensional FEA model for the baseline generator was developed in ATLAIR-FLUX.[42] One sector of the machine—comprising five poles and six slots with an odd periodicity boundary condition—was modeled. The magnets were modeled as solid two-dimensional (2D) conductors with their electrical resistivity representing a conducting medium to account for circulating eddy currents resulting from the underlying finite-element formulation for the given slot-pole geometry. This allowed for measurement of losses in the magnets during the various operating modes using an eddy-current circuit in the FEA model. The eddy current circuit was represented using five solid conductor regions. Each of the five conductors were also connected to high values of resistances in parallel to decouple the eddy currents from adjacent pole regions and also to prevent significant current flow between adjacent poles.

The baseline geometries for magnets and for core and conductor regions were modeled using line segments and arc features available within FLUX's modeler environment. Any changes to pole shape and core geometry were separately implemented using the bézier approach and parametrization (described in Section 3.1). The CAD models for each parametrized design were generated using the application programming interface capabilities of OpenCASCADE.[43] Each design included changes to the shapes for both the magnet and the back iron region for one pole whose geometry was repeated five times for one periodicity (36°) and then imported into FLUX for analysis. The different geometries were realized by a DoE approach considering the influence of the different shapes on the overall generator performance.

To capture the performance sensitivities to changes in pole shape and core geometry at a reasonable level of fidelity and accuracy, we examined three cases via 2D FEA evaluations: (a) normal operation, (b) stalling, and (c) a three-phase symmetric short-circuit fault with the turbine operating at 150 rpm. Considering the multiphysics nature of the problem, we used a decoupled approach. We first ran a transient magnetic FEA by simulating a 36° rotor rotation in the counter-clockwise direction and extracting key performance parameters including the power generated (P_{gen}), the minimum flux density in the magnets (B_{min}), cogging torque (T_{cog}), the losses in windings (P_{Cu}), the iron losses in stator (P_{Stator}), and joule losses in the solid rotor core (P_{Rotor}). This process was followed by a steady-state thermal analysis to measure the temperature rise in the winding and magnets by assuming them as thermally conducting heat sources with constant values for losses. The machine is cooled by natural convection; hence, the convection coefficients applied to the inner boundary of the stator corresponded to the static air (2.5 W/m² · K) and that of the air gap corresponded to the air flow at 150 rpm (33.19 W/m² · K). The maximum winding current density was limited to 6 A/mm².

Also, considering the weaker magnetic properties with printed polymer-bonded magnets, slightly larger currents were drawn through the windings and were calculated for the target torque needed (assuming the vector control approach) to achieve the same output power as the baseline generator. This was done by using a magnetostatic simulation to obtain and resolve the $d - axis$ components of flux linkages by Clarke's transformation and computing the current needed based on target torque. We repeated these steps for stalling and short-circuit conditions.

3 | METHODOLOGY

The first step to optimization was defining the design domain. For the rotor, we assumed the regions within the angle subtended by one pole pitch were the design space. For the stator, we chose to restrict the design exploration to only the back-iron region within the angle subtended within one pole pitch. We chose this approach because of the high degree of performance sensitivity to shape changes in any other regions in the stator

TABLE 3 Magnetic and mechanical properties of printed electrical steel.

Parameters	Rotor steel	Stator steel
Initial relative permeability	1663	12690
Saturation magnetization (T)	2.18	2.005
Knee-adjusting coefficient	0.78	1.95
Lamination thickness (mm)	—	0.35
Stacking factor	—	95%
Isotropic resistivity ($\Omega \cdot m$)	9.7E-08	1E-07
Mass density ($kg \cdot m^{-3}$)	7600	7600
Tensile strength (MPa)	485−655	650

including the stator slots, teeth, and stator conductors. Any shape change implemented within one pole pitch was patterned along the circumference. The design domains for the rotor and stator were parametrized separately to generate sufficient samples of designs and to better understand the performance sensitivities by a DoE. We used three approaches for parametrizing the rotor core and magnet regions and two approaches for the stator back-iron regions, which are discussed in the following sections.

3.1 | Shape parametrization

For the purpose of parametrization, bézier curves were chosen for their relative ease in alterations to geometry and because they require fewer control parameters using small-scale optimization algorithms, such as sequential quadratic programming.[29] Although, NURBS and B-spline-based models are also used in shape optimization of electric machines,[27,28] they involve the use of basis functions, knot vectors, and shape derivatives for shape sensitivity that add a layer of complexity. Also, achieving local control with such curves can be difficult, since each control point influences several segments. Bézier curves, on the other hand, possess favorable properties such as C1 smoothness (continuity of first derivative) at the nodes connecting segments and better localized control. Shapes obtained with Bézier curves will not require additional effort for smoothing and are compatible with CAD manufacturing software (e.g., for those used with 3D printers) making them ideal for design and production.

We consider three different parametrization approaches using Bézier curves that were introduced by Sethuraman et al.[41]: *symmetric*, *asymmetric*, and *multimaterial asymmetric* parametrizations. These parametrizations altered only the radial boundaries of the different regions. The shape changes were consistent along the axial length, and the sides of the magnets were assumed to be flat or unchanged in terms of shape. The symmetric approach defines only one half of the pole pitch, whereas the other half is a mirrored image about the pole symmetry axis. The asymmetric approach assumes shape variability across the entire pole pitch. The multimaterial asymmetric approach assumes a hybrid hard magnet realized by arranging magnets obtained by two different manufacturing methods: sintering and 3D printing arranged in a layered fashion. While the printed hard and soft magnet materials are allowed to assume shape variability across the entire pole pitch, the sintered magnet will be arc shaped. The degree of polynomial is a crucial part of ézier curve generation because it determines the complexity of shapes that can be defined using de Casteljau's algorithm in Equation (1).

$$B(t) = \sum_{i=0}^{n} P_i b_{i,n}(t), \quad t \in [0,1],$$ (1)

where $b_{i,n}(t)$ is a set of Bernstein basis polynomials of degree n given by the following:

$$b_{i,n}(t) = \binom{n}{i}(1-t)^{n-i}t^i, \quad i = 0,...,n.$$ (2)

Because de Casteljau's algorithm is recursive, we can build bézier curves of arbitrary order; however, in practice, many points are not always better. We used the 5th degree and 10th degree curves for the symmetric and asymmetric parametrizations, respectively. This choice was based on our initial judgment that controlling one half of a pole requires fewer points than a full shape in an asymmetric pole (six control points for a 5th degree curve and 11 control points for the 10th degree curve). This choice also allowed reasonable complexity and smoothness to be realized within $3.6°$ representing one half of a pole pitch and $7.2°$ representing the full pole pitch. The use of a higher-order Bézier curve offers greater flexibility and can sometimes lead to oscillatory designs. This problem was overcome by eliminating extreme shapes from an analysis of results from DoE and a careful choice of bounds for control points and their placement relative to the actual curve shape.

For each approach, we used two to three Bézier curves with control point coordinates that were allowed to vary within certain bounds in cartesian coordinates that were then scaled to specific circumferential positions in polar coordinates. These curves defined the boundaries for both the magnets and back iron of the core regions; therefore, it was possible to shape both both materials at the same time. A *ratio* parameter defined the ratio of actual magnet width to the total available pole width (i.e., $7.2°$). Bézier curves 1 and 2 defined the boundaries for magnet material. This approach permitted flexible shaping of both sides, that is, the side facing the air gap as well as the back-iron side of the magnet. We also attempted to shape the back-iron side of the magnet alone (assuming no change on the air-gap side) to study the effect on cogging torque as well as magnet mass reduction. The outermost boundary of the rotor was controlled using ézier curve 3.

We optimized the stator core as a subsequent step when an optimal rotor geometry was identified. The stator back-iron region bounded by 1 pole pitch was parametrized using a stator Bézier curve; CAD models were generated for the stator as well. Figure 4 shows the shape parametrization approach for the 15-kW generator.
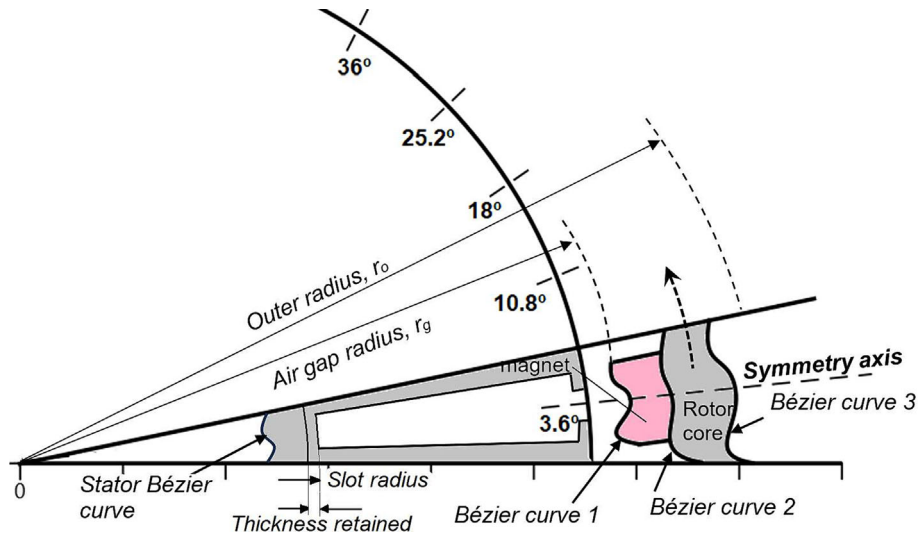
FIGURE 4 Shape parametrization for a single pole (not drawn to scale).
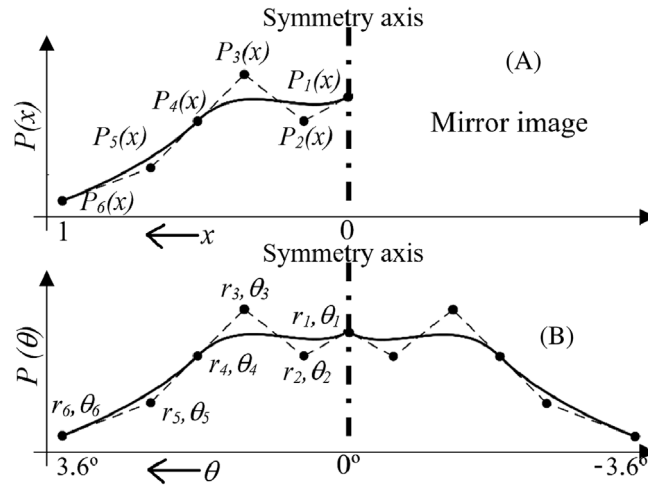
FIGURE 5 Symmetric design parameters defined in (A) Cartesian and (B) polar coordinates.

3.1.1 | Symmetric parametrization

For the symmetric rotor, we only needed to define one half of the pole using three separate fifth-order Bézier curves, each defined by six control points (as shown in Figure 5). The six control points were first normalized to be between 0 and 1 on the x-axis in the Cartesian coordinate system. They were then scaled to polar coordinates consistent with six angular increments of $\delta\theta = 0.36°$ along the rotor periphery. The Cartesian equivalent coordinates for each angular position (θ_i) are given by the radius and angle:

$$P_i(\theta_i) = r_i, \ \theta_i = P_i(x_i)\cos(i\delta\theta), P_i(x_i)\sin(i\delta\theta), \quad \text{for } i = 1,...,6. \tag{3}$$

To have a variable pole pitch, the *ratio* parameter was used to scale Bézier curve 1 accordingly,

$$P_i(\theta) = \begin{cases} P_{i+1}(x)\cos(i\delta\theta + \theta_1), P_{i+1}(x)\sin(i\delta\theta + \theta_1) \\ \theta_{avail} = ratio \cdot \dfrac{3.6\pi}{180}, \delta\theta = \dfrac{\theta_{avail}}{5} \text{ for } i = 1 \text{ to } 5 \\ P_1(x)\cos(\theta_1), P_1(x)\sin(\theta_1), \theta_1 = \dfrac{3.6\pi}{180} - \theta_{avail}. \end{cases} \tag{4}$$

To construct the shaped pole region, we evaluated Bézier curve 2 at specific positions to ensure that it started and ended at the desired points within the new interval identified for Bézier curve 1. For Bézier curve 2, we mapped the interval $\left[0, \frac{ratio}{100}\right]$ to the parameter range [0,1] using t' mapped as $\frac{t}{ratio}$ and evaluated the curve as follows:

$$B(t') = \sum_{i=0}^{n} P_i' b_{i,n}(t'), \quad t' \in \left[0, \frac{ratio}{100}\right], \tag{5}$$

where the control point, $P_i' = ratio \times P_i$, is adjusted to fit within the new interval. By applying these steps, the control points are adjusted to fit the new interval while maintaining the overall shape of Bézier curve 2. For the case with no shape change on the air-gap side, no alterations were made to the control points of Bézier curve 1.

The area under the curves, $r_{gap}(\theta)$ (i.e., the equation corresponding to Bézier Curve 1), $r_{rear}(\theta)$ (i.e., the equation corresponding to Bézier Curve 2), and $r_{out}(\theta)$ (the equation corresponding to Bézier Curve 3) obtained by integration, are doubled to obtain the mass of the symmetric magnet shapes using the respective material mass densities of $\rho_{mag} = 6150 \text{ kg} \cdot \text{m}^{-3}$ for magnets and $\rho_{core} = 7600 \text{ kg} \cdot \text{m}^{-3}$ for core.

$$Mass_{magnet} = 2 \cdot L \cdot 50 \cdot \rho_{mag} \cdot \frac{1}{2} \frac{3.6\pi}{180} \left[\int_0^{\frac{ratio}{100}} ((r_{rear}(\theta))^2 d\theta - \frac{ratio}{100} \int_0^1 ((r_{gap}(\theta))^2 d\theta \right], \tag{6}$$

$$Mass_{core} = 2 \cdot L \cdot 50 \cdot \rho_{core} \cdot \frac{1}{2} \frac{3.6\pi}{180} \left[\int_0^1 ((r_{out}(\theta))^2 d\theta - \int_0^1 ((r_{rear}(\theta))^2 d\theta \right]. \tag{7}$$

For the symmetric rotor, we consider 19 parameters including 18 control points for fine-tuning the curves along with the *ratio* parameter as input variables for creating a DoE containing a large sample set. Symmetrically shaped rotor poles were complemented with a symmetrically shaped stator back iron as well. For the stator back iron, we chose to retain a certain thickness behind the stator slot and vary the innermost boundary of the stator by using a 5th degree stator Bézier curve. The mass of the resulting back iron shape was obtained by integrating the area under the circle of radius that is smaller than the slot radius (See Figure 4) and the stator Bézier curve.

3.1.2 | Asymmetric parametrization

An asymmetric pole is defined using three distinct ézier curves of order 10, each defined by 11 control points. Note that for this case, each half of the pole need not be identical to the other (Figure 6). Similar to the symmetric approach, the initial Cartesian coordinates (0 and 1) for the control points were transformed into polar coordinates using 11 equally spaced angular intervals of $\delta\theta = 0.72°$ along the rotor periphery. Note that $P_{11}(x)$ and $P_1(x)$ are equal to retain periodicity. The available pole width was scaled using a *ratio* parameter as $\theta_{avail} = ratio \cdot \frac{7.2\pi}{180}$. The angular increments for the 10 positions were then computed as $d\theta_{avail} = \frac{\theta_{avail}}{10}$. The first control point is located at $\theta_1 = \frac{7.2\pi}{180} - \theta_{avail}$. We adjust Equation (6) to account for the entire 7.2° span of the pole arc; however, the factor of 2 is not used. This results in 31 free parameters to be considered, including
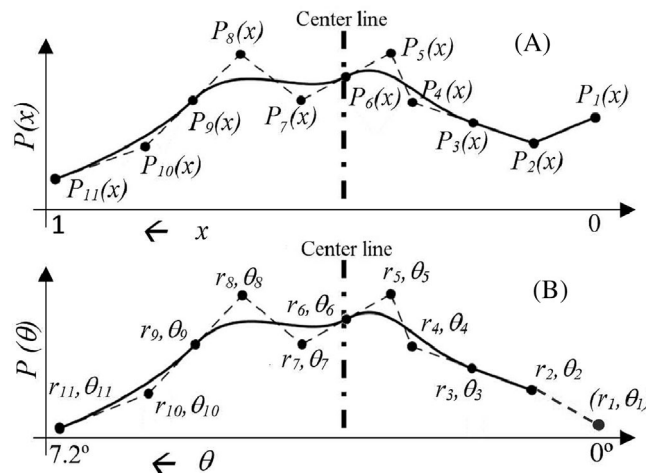
FIGURE 6 Asymmetric design parameters defined in (A) Cartesian and (B) polar coordinates.

11 control points for each of the three curves with one end point fixed by the periodicity constraints and the *ratio* parameter. We obtained the asymmetric stator back iron by using a similar approach with a separate Bézier curve parametrized using 11 control points.

3.1.3 | Multimaterial asymmetric parametrization

Figure 7 shows the parametrization approach for one magnet pole. The magnet region is modeled using a new layering technique with two different materials (Magnets 1 and 2) manufactured by sintering and 3D printing. The bottom layer (Magnet 1) is modeled as an arc-shaped sintered magnet of certain thickness (h_{m1}). The top layer (Magnet 2) was modeled as printed, polymer-bonded magnet. This second layer will be printed by FDM and overmolded to the layer of sintered magnet and rotor core. While these layers can be interchanged, the sintered magnet was placed in the ar gap side to make use of its higher knee point (0.45 Tesla). Two parameters, namely, h_{m1} and *ratio*, were varied to optimize the shape of sintered magnet layer. The printed magnet was shaped only on its back side in order to make a flat surface available for easy bonding to sintered magnet material. Two 10th degree Bézier curves each with 11 control points formed one pole. The mass of the magnet was computed using the approach discussed earlier by applying the different mass densities for the respective magnets ($\rho_{mag1} = 7600 \, \text{kg} \cdot \text{m}^{-3}$ and $\rho_{mag2} = 6150 \, \text{kg} \cdot \text{m}^{-3}$). For the DoE evaluation, 22 variables were considered including 11 control points for each of the two curves with the periodicity constraint enforced, h_{m1}, and the *ratio* parameter.

4 | DESIGN WORKFLOW

We begin the optimization workflow with a random set of control points of Bézier curves and the *ratio* parameter generated by Latin-Hypercube sampling technique[44] available in Python's PyDOE2 package.[45] Each of these samples results in a distinct shape with a certain magnet and core mass (Figure 8). An initial DoE is performed with 1000 sets of control points. For each of the 1000 sets, seven different *ratio* parameters in increments of five were picked from the range of 60–90. The purpose of the DoE was to evaluate the different design sensitivities without the need for shape derivatives. This was done by performing transient magnetic analysis followed by thermal analysis in steady state using FLUX. We extracted the simulation results and then used the mass criteria with the targets defined in Table 4 to sort and filter the designs. For single-magnet designs, Bézier curve 1 was used as reference to control the shapes on Bézier curves 2 and 3 using the bounds as shown in Tables 5 and 6. Thus, both magnet and rotor core boundaries were simultaneously controlled. For the multimaterial magnet designs, we used a constant magnet thickness of h_{m1} to define the starting boundary for the printed polymer-bonded magnet and the lower bound for Bézier Curve 1 (Table 7). Bézier curve 2 represented the outer boundary of the rotor core that was accordingly sampled. The multimaterial magnet optimization was restricted to the rotor design alone (i.e., only rotor that was parametrized with baseline stator). Each of the rotor designs (defined by their control points) was imported into OpenCASCADE[46] using its application programming interface. The 2D CAD model for a single pole was generated and then a circular repetition of the single pole was created for one periodicity (36°) using PythonOCC.[43] We imported the CAD models into FLUX and solved for three operating cases, as defined in Section 2.2, and extracted performance parameters. The dataset, especially for symmetric designs, had very few cases that satisfied all performance criteria, and to help realize higher mass reduction, we chose to use an adaptive sampling approach (see Section 4.1) to refine the DoE.
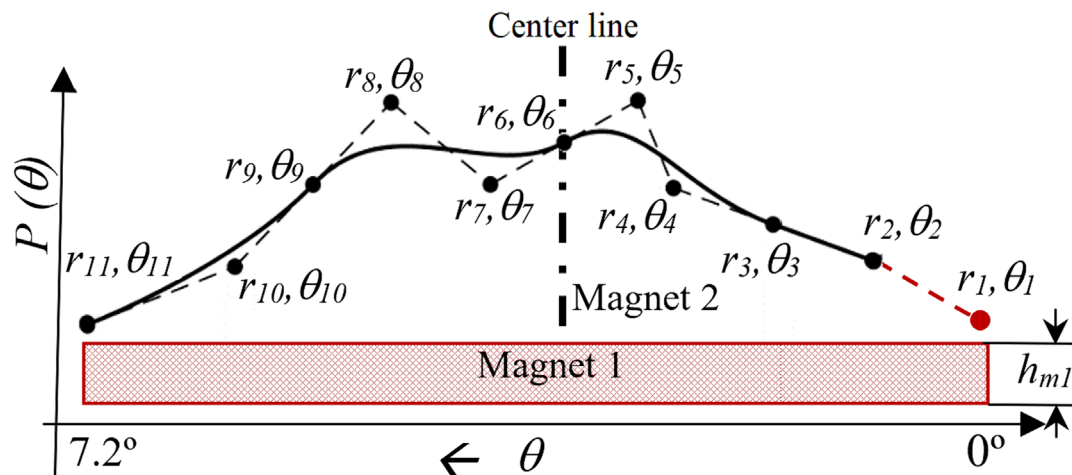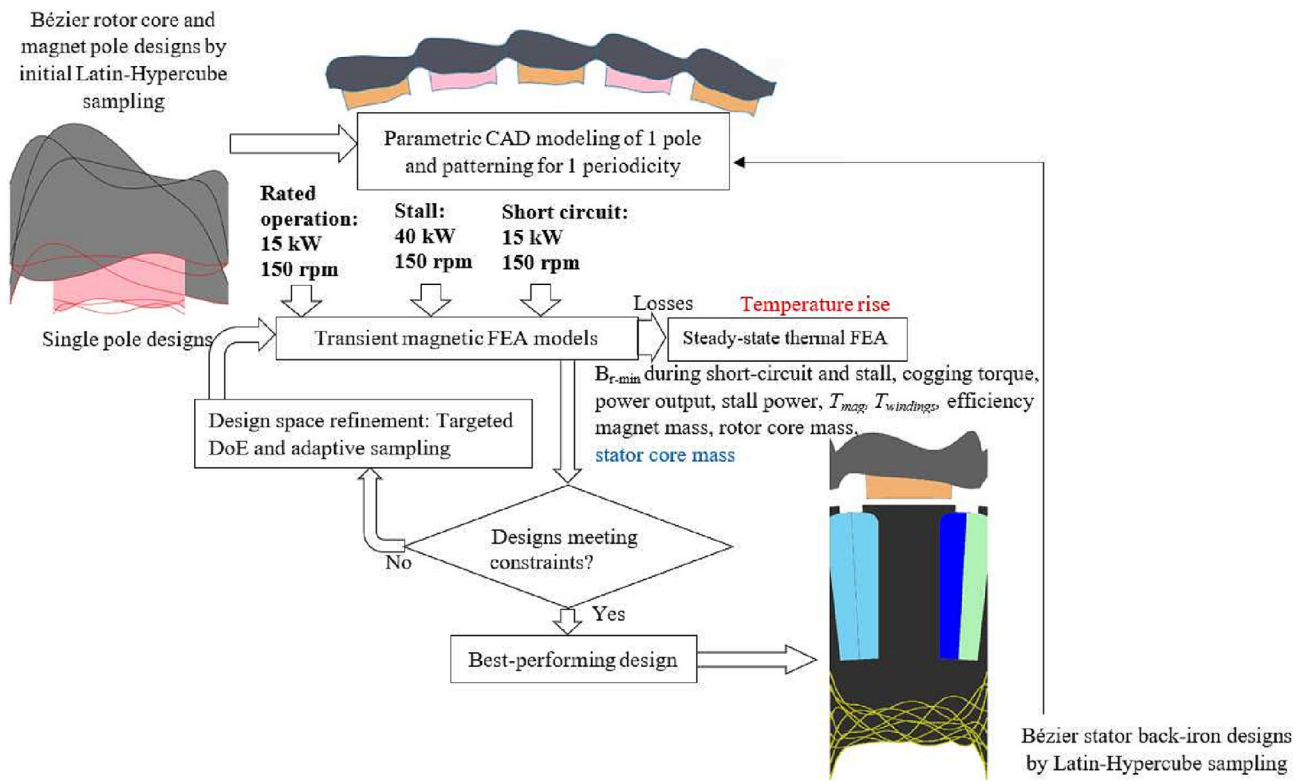

FIGURE 7 Multimaterial parametrization that combines Bézier control points with a standard magnet shape.

FIGURE 8 Design of experiments approach.

TABLE 4 Design optimization targets.

Parameters	Symbol	Units	Baseline	Target
Air-gap radius	r_g	mm	287.1	≥ 287.1
Core length	l	mm	150	150
Rotor outer radius	r_o	mm	303.53	$\leq r_g + 30$
Stator inner radius	r_{stator}	mm	227.5	≥ 227.5
Inner radius limit	r_{inner}	mm	240.5	240.5
Pole arc/pole pitch	ratio	%	Proprietary data	$60 \leq ratio \leq 100$
Rated voltage	V	V	≤ 575	≤ 575
Efficiency	η	%	95	≥ 95
Cogging torque	T_{cog}	Nm	33	≤ 25
Magnet mass	M_{mag}	kg	7.31	≤ 6.58 (>10% reduction)
Minimum magnetization	$B_{rmin-SCandstall}$	T	0.45	0.3
Winding temperature	$T_{winding}$	°C	180	180
Magnet temperature	T_{mag}	°C	60	60

We identified the best-performing rotor design from the adaptive sampling approach using the target values defined in Table 4 and used them to conduct a subsequent optimization of the stator back iron. The stator back-iron shapes were also generated using randomized sampling of control points by Latin-Hypercube sampling similar to the rotor region with more than 1000 samples. CAD models were generated as well. Note that the symmetric and asymmetric rotor poles were matched with symmetric and asymmetric back-iron shapes. A second round of transient, magneto-thermal FEA simulations were performed, and the key performance parameters were extracted with the shaped stator back iron. The best-performing designs were extracted from the DoE, and final optimal symmetric and asymmetric designs were identified. Once the optimal shape of magnetic materials was identified for the design, we evaluated its air-gap stiffness using static structural analysis in SolidWorks.[47]

4.1 | Adaptive sampling

To improve the performance of the generated designs and refine the design space exploration with an augmented dataset that better reflects desirable design characteristics, we implemented two forms of adaptive sampling that focus on regions of the design space (i.e., the parameter space) that correspond to high-performing designs. In general, adaptive sampling is an iterative framework that uses insights from previous rounds of sampling to better explore the parameter space with respect to various targets (e.g., enhanced metamodeling, reduced uncertainty, improved optimization, etc.).[48] The first form of active sampling leverages subspace-based dimension reduction of the input parameters to define linear inequality constraints that focus on target values listed in Table 4. We mostly used this approach for asymmetric designs that had more flexibility in design exploration. The second approach extends insights from the flexible asymmetric design space to the more restricted symmetric design space.
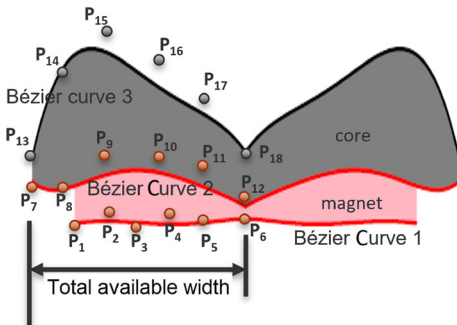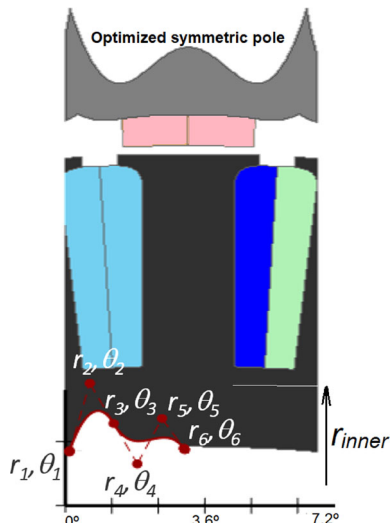
4.1.1 | Subspace-based sampling

To inform a more efficient sampling scheme, we sought a reduced subspace of the full parameter set that captured most of the variation in our target outputs. In general, given a vector of high-dimensional input parameters $x \in \mathbb{R}^n$ and corresponding model outputs $f(x) \in \mathbb{R}$ data, we can identify a low-dimensional structure using a variety of methods, including active subspace[49] and inverse regression.[50] For this work, we leveraged a polynomial ridge approximation technique to uncover this low-dimensional structure.[51] This approach solves a joint minimization of a d-degree polynomial approximation, $\tilde{f}$, defined over a p-dimensional subspace determined by $W \in \mathbb{R}^{n \times p}$,
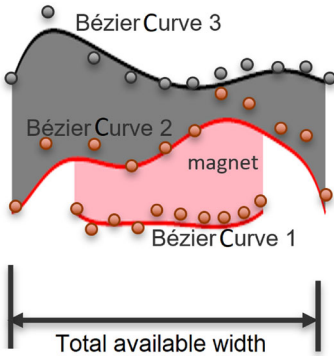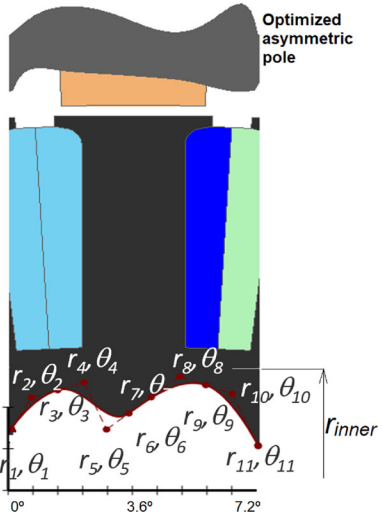
$$\min_{\substack{W \in V_p(\mathbb{R}^n) \\ \tilde{f} \in \mathcal{P}_d}} \left\| f(x) - \tilde{f}(W^\top x) \right\|_2^2. \tag{8}$$

In practice, this complex joint optimization is solved by recasting the problem as a minimization over the orthogonal projection of the Vandermonde matrix of the polynomial approximation.
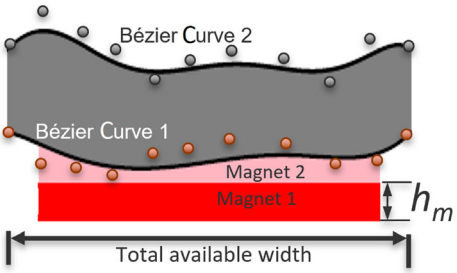
TABLE 5 Symmetric rotor and stator parametrization.

Methods	Symmetry rotor		Symmetry stator	
Exable design				
Order of the curve (n)	5th		6th	
Curve 1: $P_{i,i+1,..,n}$	Lower bound	Upper bound	Lower bound	Upper bound
	$r_{i,i+1,...,n} \geq r_g$	$r_{i,i+1,...,n} \leq r_g + 5$	$r_{i,i+1,...,n} \geq r_{stator}$	$r_{i,i+1,...,n} \leq r_{inner}$
	$\theta \in 0, 3.6°, \delta\theta = 0.6°$	$\theta \in 0, 3.6°, \delta\theta = 0.6°$	$\theta \in 0, 3.6°, \delta\theta = 0.6°$	$\theta \in 0, 3.6°, \delta\theta = 0.6°$
Curve 2: $P_{n+1,n+2,...,2n}$	$r_{i,i+1,...,n} \geq r_g$	$r_{n+1,n+2,...,2n} \leq r_g + 10$	Curves from optimized symmetric pole	
Curve 3: $P_{2n+1,2n+2,...,3n}$	$r_{n+1,n+2,...,2n}$	$r_{2n+1,2n+2,...,3n} \leq r_g + 30$		
$ratio\left(\frac{Actual\,pole\,width}{Total\,available\,width}\right)$	60	100	$ratio_{opt}$	

TABLE 6 Asymmetric rotor and stator parametrization.

Methods	Symmetry rotor		Symmetry stator	
Example design				
Order of the curve (n)	10th		10th	
Curve 1: $P_{i,i+1,..,n}$	Lower bound	Upper bound	Lower bound	Upper bound
	$r_{i,i+1,...,n} \geq r_g$	$r_{i,i+1,...,n} \leq r_g + 5$	$r_{i,i+1,...,n} \geq r_{stator}$	$r_{i,i+1,...,n} \leq r_{inner}$
	$\theta \in 0, 7.2°, \delta\theta = 0.72°$	$\theta \in 0, 7.2°, \delta\theta = 0.72°$	$\theta \in 0, 7.2°, \delta\theta = 0.72°$	$\theta \in 0, 7.2°, \delta\theta = 0.72°$
Curve 2: $P_{n+1,n+2,..,2n}$	$r_{i,i+1,...,n} \geq r_g$	$r_{n+1,n+2,...,2n} \leq r_g + 10$	Curves from optimized symmetric pole	
Curve 3: $P_{2n+1,2n+2,..,3n}$	$r_{n+1,n+2,...,2n}$	$r_{2n+1,2n+2,...,3n} \leq r_g + 30$		
$ratio\left(\frac{Actual\,pole\,width}{Total\,available\,width}\right)$	60	100	$ratio_{opt}$	

TABLE 7 Multimaterial asymmetric rotor parametrization.

| Methods	Multimaterial asymmetric rotor	
Example design		
h_m	Lower bound	Upper bound
h_m	1.5	9
Order of the curve (n)	10th	
Curve 1: $P_{i,i+1,..,n}$	$r_{i,i+1,...,n} \geq r_g + h_{m1}$	$r_{i,i+1,...,n} \leq r_g + 10$
Curve 2: $P_{n+1,n+2,..,2n}$	$r_{i,i+1,...,n}$	$r_{n+1,n+2,...,2n} \leq r_g + 15$
$ratio\left(\frac{Actual\,pole\,width}{Total\,available\,width}\right)$	60	100

Active parameter and shape sensitivity

In the context of the design problem discussed in Section 3, the main input parameters *x* are the Bézier control points that define the magnet shape—that is, the P_i coefficients from Equation (1). The reduced parameter representation $W^\top x$—also referred to as the *active parameters*—define(s) a new basis expansion in terms of the linear combination of the current Bézier expansion that captures the most variability in the output

f using $p < n$ parameters. Note that for the target sampling work, we focus on the $p = 1$ scenario such that we correlate different outputs against a single active parameter. We consider multiple different output quantities for the subspace-based sampling analysis—namely, the magnet and core masses and the efficiency, magnetization, and the cogging torque. We also examine low-dimensional relationships for other outputs of interest, including the air-gap flux density and output power.

Our subspace-based sampling approach takes the identified *active parameter* for each output and uses it to apply linear inequality constraints that filter the parameter space to target values. Figure 9 shows a collection of shadow plots—scatter plots of the various output quantities of interest against their low-dimensional *active parameter*.[52] Recall that these active parameters define reparametrizations of the basis expansion from Equation (1) resulting in shape variations that have the largest impact on each output quantity. To complement these shadow plots,
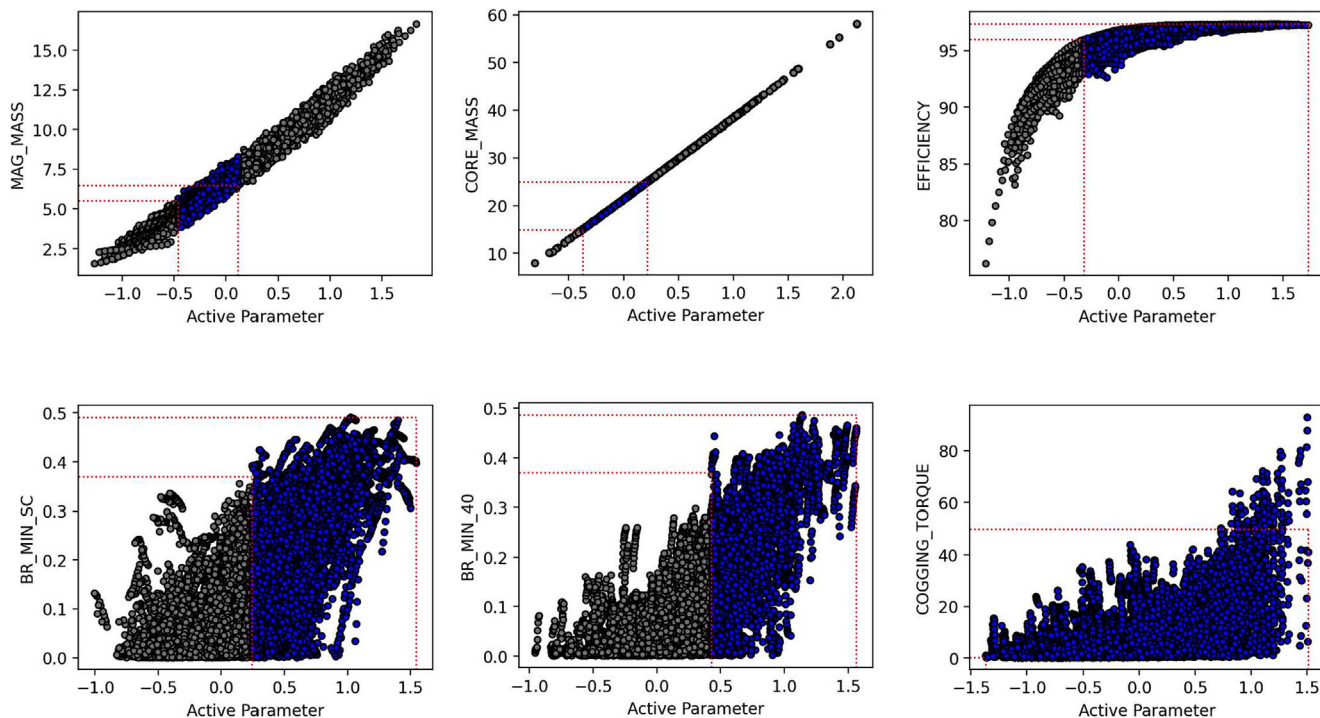
FIGURE 9 Shadow plots depicting the low-dimensional subspace projections for various output quantities with thresholds applied to targeted values to obtain a reduced design space that can be readily subsampled.
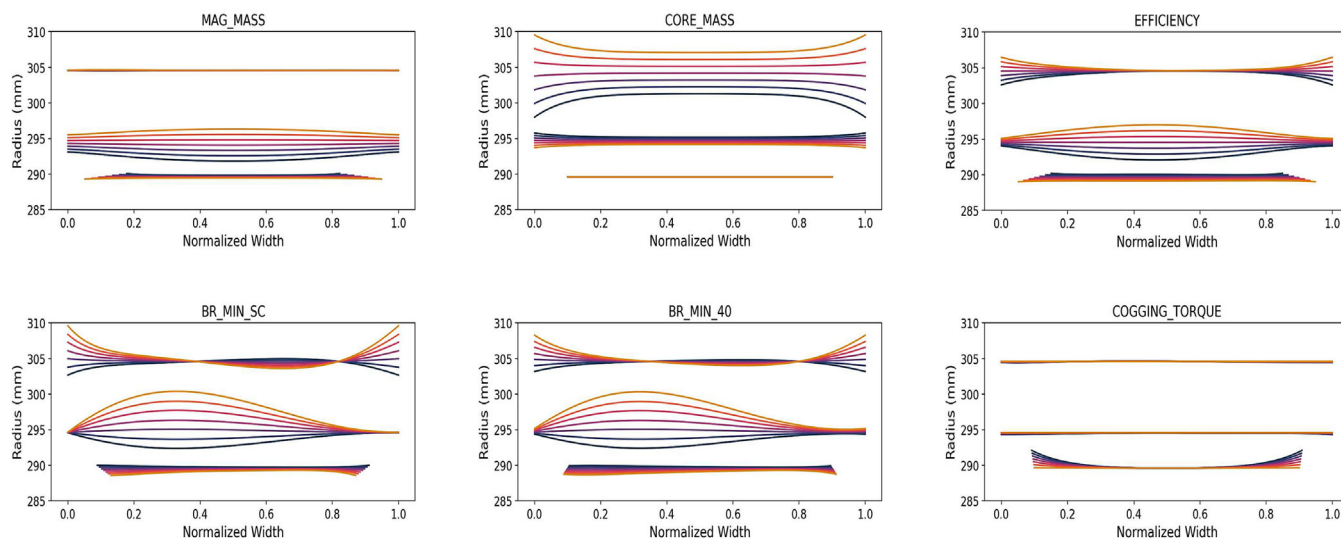
FIGURE 10 Magnet designs resulting from sweeps across each active parameter from Figure 9. The transition from blue to yellow shapes corresponds to traversing from the minimum value of each active parameter to the maximum.

Figure 10 visualizes the changes to magnet designs that occur by sweeping across each active parameter from its lowest value (in blue) to its highest value (in yellow). These sweeps help to characterize the sensitivities in performance to the different shapes of the magnets.

For example, the design with highest efficiency (i.e., highest value of the active parameter) always tends to be convex shaped in the center of the magnet pole suggesting most power losses occur if the rear side of the magnet is concave. Similarly, the designs with the lowest cogging torque (the smallest value of the active parameter) are more rounded toward both the edges of the magnet. The smallest magnet and rotor core masses always corresponded to the thinnest magnet and core regions. To achieve a high peak air-gap flux density (see bottom left plot in Figure 11), the rear-side of the magnet should curve outward with the center of the magnet being thicker than its edges. In contrast, the magnet shape starts to be more asymmetric, that is, thicker on the left side than the right side to achieve higher stall power, higher $B_{rmin-SC}$, and $B_{rmin-stall}$.

Considering these multiple shape sensitivities, a filter was applied to specific output quantities (horizontal red lines) to highlight samples within a targeted range of values and then mapped down to the filters over the *active parameter* (vertical red lines). Using these filters, we defined a set of inequality constraints to be applied to a subsampling of the design space (blue scatter points in Figure 9). Note that the "tightness" of the scatterplot indicates the accuracy of the low-dimensional approximation. For the mass quantities, the low-dimension representation is strong so that the targeted range of active parameters correlate well with our desired output quantities. Other quantities provide looser bounds that can still result in undesirable quantities; however, the applied filters ensure that we avoid regions of the parameter space where we did not see any valid data points. Overall, we reduced the overall size of the parameter space by more than 99% using this subspace-based approach to adaptive sampling. This procedure is iterated as necessary to identify the final optimal asymmetric design.
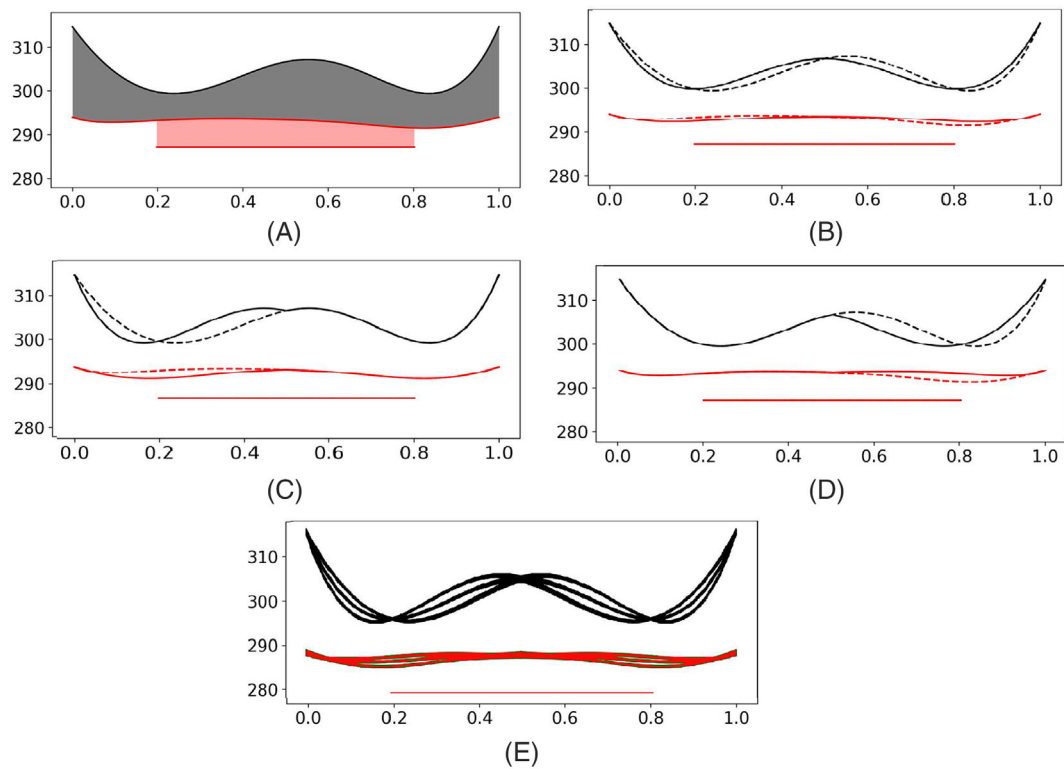
4.1.2 | Reconstructing symmetric designs

The second adaptive sampling approach leveraged insights from the asymmetric DoE to help enhance the more restrictive symmetric DoE. Despite the large number of symmetric designs that were generated, very few actually satisfied the performance targets. Therefore, we identified a lightweight asymmetric pole design that closely resembles a symmetric pole such that it could be manipulated to generate new symmetric designs. This adaptive sampling approach created three symmetric shapes that approximated this asymmetric baseline by obtaining symmetric Bézier control points that minimized reconstruction errors for (i) overall shape, (ii) the right-hand side, and (iii) the left-hand side. In Figure 12, we see the baseline asymmetric design (dotted lines) along with each of these symmetric approximations (solid lines). We then added 100 new samples by performing ± 10% perturbations to the controls points around each of these new symmetric targets. The optimal symmetric design was identified from a DoE with the new samples.
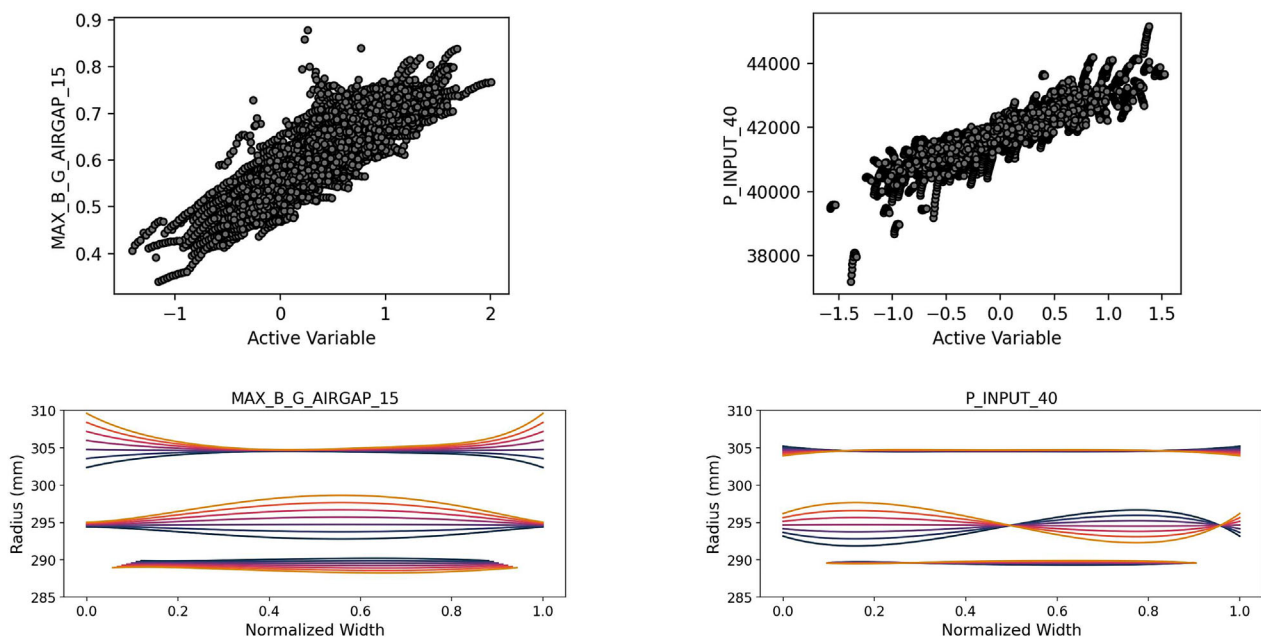
FIGURE 11 Top graphic: Sensitivity of peak air-gap flux density and stall power to their respective active parameters. Bottom graphic: Shape sensitivities of peak air-gap flux density and stall power visualized against normalized pole width. The transition from blue to yellow shapes corresponds to traversing from the minimum value of each active parameter to the maximum.

FIGURE 12 Constructing a symmetric design from a baseline asymmetric design: (A) an asymmetric baseline shape that is near-symmetric, (B) a symmetric shape obtained by minimizing the overall reconstruction error of the baseline, (C) a symmetric shape obtained by minimizing the reconstruction error of the right-hand side of the baseline, (D) a symmetric shape obtained by minimizing the reconstruction error of the left-hand side of the baseline, and (E) 100 new symmetric shapes obtained from ± 10% perturbations to the three symmetric approximations of the asymmetric baseline.

4.2 | Structural optimization

With the generator rotor profile complete, it is necessary to transition the 2D optimized profile into a manufacturable 3D design. For the structural analysis, we chose to extrude one of the 2D optimized designs into a 3D model in SolidWorks. An optimized design with an asymmetric pole (Case III) was chosen for this effort to evaluate a combination of magnetic asymmetry with structural symmetry. The support structure is a cylindrical structure with double-sided disks that is mounted onto a shaft and supported by front and rear bearings (See Figures 13 and 14). The cylindrical structure features two overhangs on either side of the asymmetric profiling for the active portion of the generator's stack length. Magnets are held on the inside (See Figure 14). The main goal of this exercise was to optimize the rotor's structural mass while ensuring the stiffness to resist deformation caused by the blade loads and air-gap forces from the magnets. A key parameter of interest in this study is the radial stiffness-to-weight ratio because it is critical to maintain the air gap between the magnets and stator teeth. The objective is to maximize stiffness-to-weight, which will occur when the system stiffness is maximized and the weight is minimized. We applied several constraints on the optimization such that the result would have minimal impacts on manufacturing, operation, and maintenance. First, to provide ingress protection for the generator, no holes or openings were allowed in the geometry of the disk (other than necessary bolt holes). Any optimization should also ensure easy access for installation and maintenance of the generator from the back side of the rotor. Also, the inside of the rotor had to be constrained to be as uniform as possible. Finally, the maximum deformation for the radial direction was constrained to be 0.38 mm and to be 6.35 mm for the tangential and axial directions.

4.2.1 | Applied loads

The generator and blade assembly is shown in Figure 13. The blades and reinforcement brackets are bolted to the front with a face plate. The generator assembly is constrained in five degrees of freedom with the front bearing assembly. Note that the front bearing assembly, as designed by the OEM, supports all of the thrust forces and the majority of the torsional loading. The rear bearing assembly, while not strictly necessary for
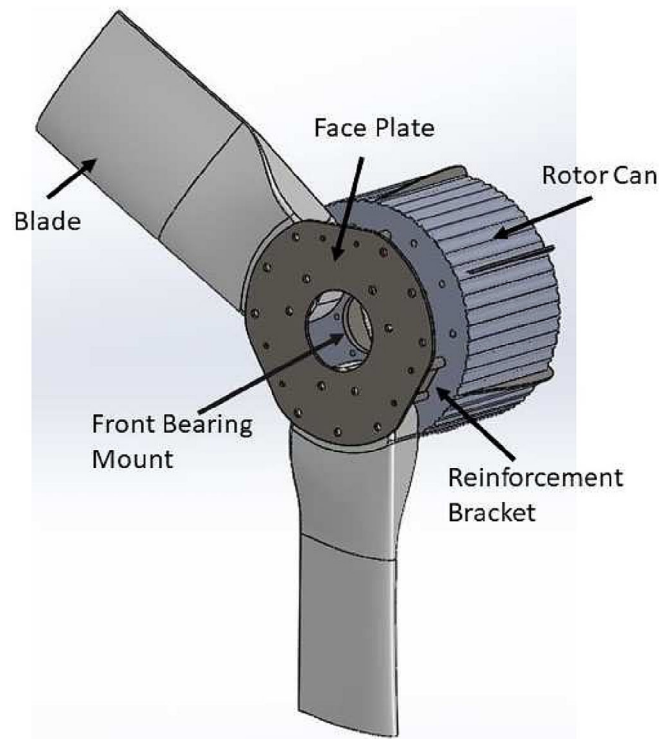
FIGURE 13 Generator assembly with components labeled. The blades are modeled as blade sections to reduce computational load. There are three blades (one blade has been hidden from view) and reinforcement brackets are attached to the front of the generator with the face plate and bolts (not shown). The front bearing is mounted to the front of the rotor can.
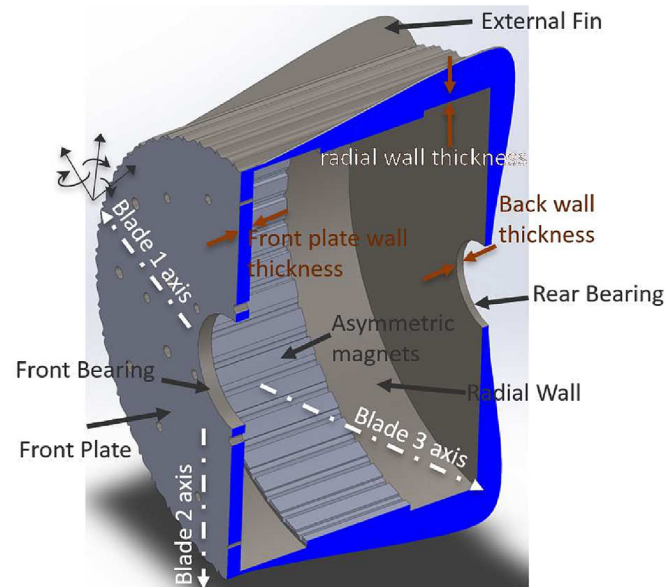
FIGURE 14 Structural parametrization of the rotor can.

operation, supports pitch and yaw moments. The blade assembly with the reinforcement brackets and face plate creates a very stiff assembly that provides the necessary strength and rigidity to react to the translational and rotational loading from the blades. Additionally, with the majority of loads acting on the front bearing, the rear bearing can be smaller and have fewer supporting structures around it. This not only reduces cost but also facilitates assembly and maintenance procedures by reducing the weight of the components.

We extracted the blade loads from the FAST simulation of a similar previously deployed 15-kW wind turbine. We measured translational forces with respect to the generator's axis of rotation (AoR) in cylindrical coordinates. Additionally, we calculated moments acting on each blade relative to the blade axis with Axis 1 along the chord, Axis 2 perpendicular to the blade, and Axis 3 along the length of the blade. See Table 8. These loads were taken from real-world wind loading data and are highly asymmetric. Although this complicates the optimization, we decided to keep the nonuniform loading to better reflect deployment conditions. The magnets pull radially inward toward the AoR due to the interaction between them and the stator. Finally, gravitational acceleration is applied to all bodies at seven degrees above horizontal as is experienced by similar installed units.

Although the rotor cross-section is locally asymmetric around each pole, it is globally (i.e., around the entire rotor) uniform. Therefore, the center of gravity is unaffected and will not induce any nonuniform radial or vibrational loading. Further, vibrational loading has been investigated by the OEM but is not considered to be significantly impacted by the rotor lightweighting and hence was not included in the scope of this work.

4.2.2 | Methodology

Figure 14 shows a sectional view of the inside of the generator rotor with the magnets and some overhang on either side. Two flat disks on the front and rear ends are used to seal the generator. With the main constraints identified in Section 4.2 already limiting the design space to some extent, we parametrized some dimensions and developed a series of features to either increase stiffness or decrease the mass. Figure 14 shows the main parameters including the thicknesses for the radial wall, front and back plate, and the number and thickness of radially distributed external fins with bounds shown in Table 9. A two-level, full-factorial design of experiments (FFDoE) was performed, and a linear regression model was constructed using the data that were used to optimize the stiffness-to-weight ratio. In total, there are six factors and two levels per factor for $2^6 = 64$ treatment combinations. Because of computation time and costs, this was the practical limit for this analysis. Please note that only the rotor was evaluated from a structural stiffness point of view. For the stator with shaped back iron, the lamination stacks are expected to be made in segments with each segment representing 1/10 of the full machine (as shown in Figure 3). While such a shaped back iron will also need a new support structure design, such a study was not considered for the present scope and shall be evaluated as part of a future study.

We performed static FEA simulations in SolidWorks 2022[47] with the design study feature. For the simulations, the front bearing surface was treated as a fixed constraint while the rear bearing had a cylindrical constraint that allowed it to move axially while translation and rotation were constrained. The front and rear bearing surfaces were connected together with a pinned constraint to simulate the generator shaft by enforcing concentricity. These are the only fixtures that were identified to accurately simulate the loads acting on the rotor. The nature of magnetic loading for the asymmetric pole design is that of a uniformly varying load (UVL) that is also periodic (see section for details). For studying the impact of

TABLE 8 Loads acting on the generator rotor.

Forces/moments	Units	Blade 1	Blade 2	Blade 3	Blade axes
Radial force (away from AoR)	N	433	252	226	
Tangential force (counterclockwise from AoR)	N	519	339	554	
Axial force	N	3243	3429	3294	
Moment about Axis 1	Nm	3647	3338	4055	
Moment about Axis 2	Nm	966	196	789	
Moment about Axis 3	Nm	258	409	211	
Maxwell pressure from magnets	MPa		0.13		

TABLE 9 Parameters and levels for the two-level FFDoE.

Parameter	Low level	High level	Baseline
Front plate thickness (mm)	6.35	15.875	19.05
Back plate thickness (mm)	3.175	9.525	9.525
Radial wall thickness (mm)	3.175	9.255	10.312
Fin height beyond can outer wall (mm)	25.4	50.8	NA
Fin thickness (mm)	3.175	6.35	NA
Fin quantity	0	6	NA

such magnetic loading on the radial stiffness of the rotor, we studied one case of peak pressure (0.13) MPa and applied it to the internal surface of the rim. Very little material was removed from the rotor core by magnetic optimization, and the radial stiffness is very similar to that of the baseline support structure, so the stiffness behavior is expected to be minimally impacted by the pressure variation caused by asymmetry. This is because even the highest peak magnitude in the UVL (0.295 MPa) is still lower than that of the baseline design (See Figure 17). Additionally, that load repeats periodically around the rotor so it is not expected to cause asymmetric deformation.

We calculated the stiffness-to-weight ratio from the simulation outputs using Equation (9), where radial stiffness is dependent on radial stress, σ_{rad}, and radial strain, ε_{rad}. The absolute value is necessary to eliminate directionality (i.e., deformation inward or outward).The net weight, W_{net}, is predicted from volume and mass density. The maximum predicted stress and maximum predicted strain are used to find the stiffness-to-weight for each treatment combination in the FFDoE.

$$stiffness - to - weight = \frac{stiffness_{rad}}{W_{net}}, \tag{9}$$

where radial stiffness is radial stress divided by radial strain, that is, elastic modulus,

$$stiffness_{rad} = \frac{\sigma_{rad}}{|\varepsilon_{rad}|}. \tag{10}$$

We then performed an analysis of variance on the stiffness-to-weight ratio from each treatment to determine the significance of each factor. Finally, we performed a linear regression to create an empirical model for the rotor can thickness. Maximizing this function will help maximize the stiffness-to-weight and determine the best solution within this design space.

5 | RESULTS

5.1 | Magneto-thermal evaluation

We probed the results from the optimization approach we presented in reference[41] (and shown in Table 10) and also compared them with a prior study by Labuschagne et al[21] where a crown-shaped pole was optimized with an N48H-grade NdFeB magnet. All the symmetric and asymmetric designs were selectively picked from DoE such that they were the lightest in the set and delivered 15 kW during normal operation and 40 kW of stall power by not violating the demagnetization constraints. The lightest pole design weighing 4.77 kg was 35% lighter than the baseline magnet and was realized using layered magnets made of sintered and printed magnets. This design also had a higher efficiency due to substantially lower magnet losses measured with 3D printed magnets (Figure 15).

These magnet loss measurements corresponded to resistive losses from the eddy currents circulating in the magnet regions that were modeled as solid conductors (See Section 2.2). As the rotor rotated, the flux linking with these solid conductor regions changed and resulted in circulating currents. It was therefore possible to measure the associated losses as a measure of joule effect using the magnet's resistivity. The magnitudes of the peaks of eddy currents are of the order of 1.7–2.0 mA for the baseline magnets and of the order of 1.0–3.0 mA for printed magnets. Despite the slightly higher eddy currents with the printed magnet design, the resistivity of printed magnets is several orders of magnitude higher than sintered magnets (see Table 3). As a result, magnet losses with printed magnets are substantially lower.

The lightest asymmetric design (Case IV) weighed approximately 5.37 kg and resembled a trapezium. This design was 27% lighter when compared to the baseline. As the rotor rotated in the counter-clockwise direction, it was apparent that the magnet material distribution followed the rotating magnetic field, that is, the magnet is thicker on the left and thinner on the right. In the case of symmetric design (Case VI) with a constant air gap, notice the wave-like pattern with two troughs. The shaping technique identified a design that removed material from the rotor core in regions with minimal magnetic loading. Such wave-like shapes can be printed using the FDM technique, then overmolded to a printed rotor. This approach obviates the use adhesives for magnet bonding. For best results, the shape optimized rotor can be printed by SLM or using sand printing and casting. Considering the dimensions of the rotor core (with a height of 150 mm), it is possible that molten steel could have freezing issues during casting and so alternative materials such as cast iron may be used when manufacturing the rotor core. While previous studies on asymmetric poles observed issues such as unbalanced magnetic pull, the circular repetition of asymmetric designs obtained through our approach balances such internal forces. A comparison of the air-gap flux density profile between asymmetric (Case III) and symmetric designs (Case IV) in Figure 16 shows a minor offset in the peaks—although the magnitudes were comparable. Figure 17 compares the normal magnetic stress distribution in the air gap for Case III against the baseline case. Case III has smaller magnitudes in pressure peaks, which is also attributed to smaller B_r for printed magnets that uniformly varies with the magnet height (See Figure 18). The baseline rotor is mounted onto a shaft supported by two ball bearings, and it is intended to use the same system for Case III. The magnetic pressure distribution per pole in the baseline case represents a uniformly

TABLE 10 Results from rotor optimization.

Designs	Baseline design	I	II	III	IV	V	VI	VII
		Re-optimized baseline from Labuschagne et al.[21]	Crown design from Labuschagne et al.[21]	Asymmetric pole: nonconstant air gap	Asymmetric pole: constant air gap	Symmetric pole: nonconstant air gap	Symmetric pole: constant air gap	Multimaterial asymmetric pole: constant air gap
Magnet material	Sintered N52 magnet with zero dysprosium	N48H sintered magnet with zero dysprosium	55.5% weaker printed polymer-bonded magnet with zero dysprosium					
Magnet mass (kg)	7.31	4.31	6.14	5.49	5.37	6.18	5.99	4.77
Efficiency (%)	96.1	96.9	97.1	96.9	96.88	97.05	96.99	97.05
B_{rmin}(T)	0.453	0.456	0.3	0.31	0.31	0.299	0.302	0.50
T_{cog} (Nm)	25.33	24.8	24	24.21	23.18	27.5	24.78	24.105
ratio	71.62	69	65.8	64.62	60.23	65.95	60.64	68.97
Optimized design								
% magnet weight change	—	−41	−16.0	−25.0	−26.5	−15.45	−18	−35
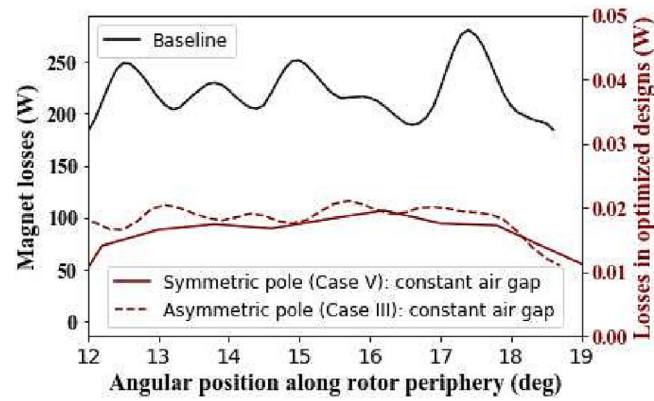
FIGURE 15   Comparison of magnet losses.
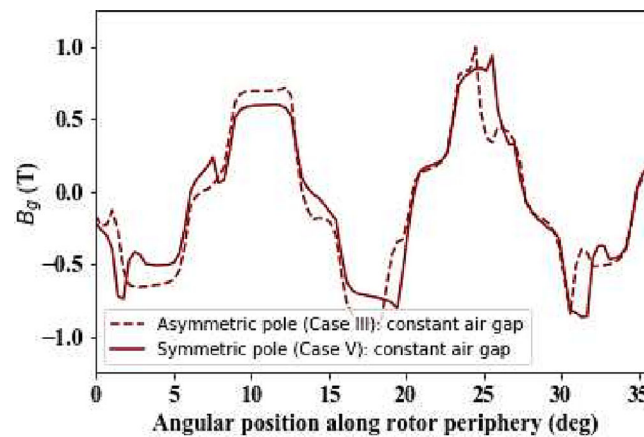
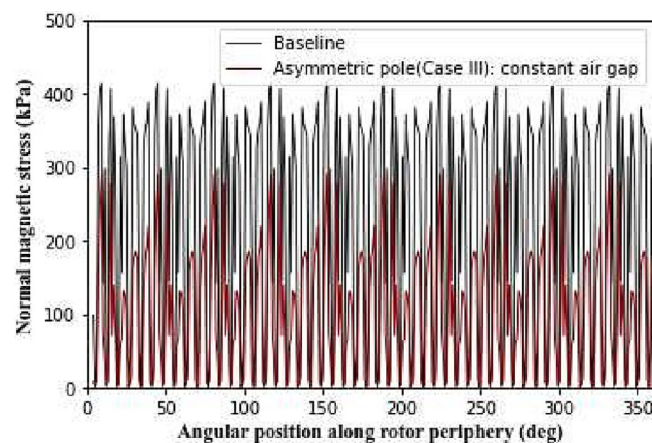**FIGURE 16**   Comparison of air-gap flux density profiles for symmetric and asymmetric poles.
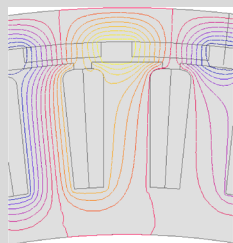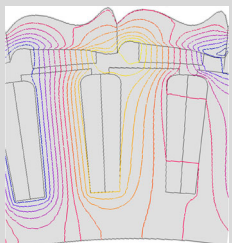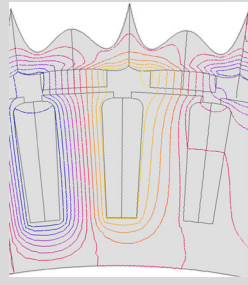
FIGURE 17   A comparison of normal magnetic pressure loading between the baseline and asymmetric designs.

distributed loading with a peak of 413 kPa. This uniform pressure translates to evenly distributed forces on the bearing raceways and rolling elements. The pressure distribution per pole in Case III presents small uniformly varying pressure that is also periodic (i.e, a pole diametrically opposite to another pole will balance the pressure load). Note that the peak pressure variation per pole is between 131 and 295 kPa that is substantially smaller in magnitude when compared with the loading in the baseline design. Therefore, the authors opine that this would not negatively impact the bearing performance. A detailed investigation on bearing lifetime is outside the scope of this work and shall be addressed as part
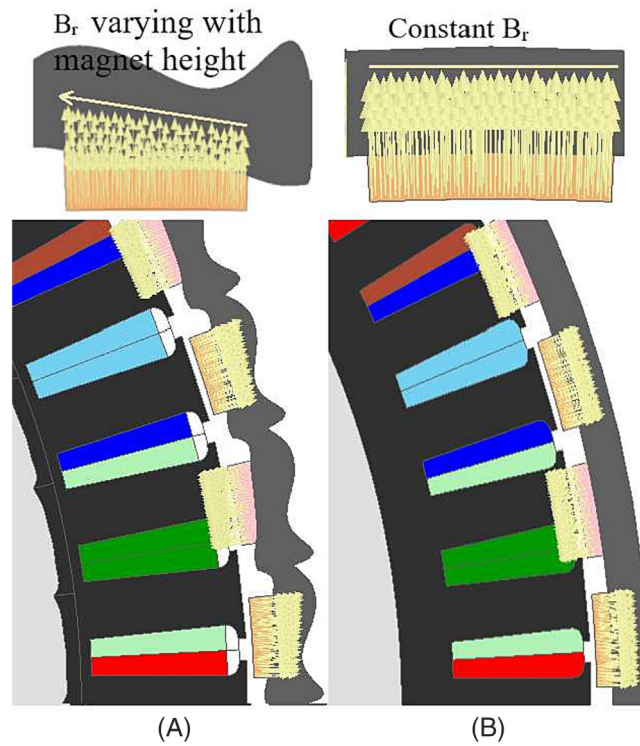
FIGURE 18 Comparison of pole remnant flux densities (A) Case III. (B) Baseline design.

TABLE 11 A comparison of characteristics between the baseline design and Cases IV and VI design.

Optimized design	Baseline design (with N48H magnets)	Asymmetric rotor and symmetric stator	Symmetric rotor and symmetric stator
Stator inductance (mH)	6.5	7.44	7.48
Rated current (A)	35.57	42.98	41.18
$B_{rmin-SC}$(T)	0.53	0.387	0.391
$B_{rmin-stall}$(T)	0.45	0.305	0.30
Terminal voltage (V_{L-L} rms)	344.33	313.2	320.87

of a future effort. A further analysis is included in the section for structural evaluation where one particular pressure case was simulated. Further, wave-like patterns on the surface of the rotor can also serve as a more effective aerodynamic element for cooling.

Table 11 compares the electromagnetic characteristics of optimized designs (Cases IV and VI) with the baseline design. The stator inductances for the optimized designs have increased and are attributed to the change in the pole geometry and length of the flux path obtained as a result of the shaping as shown in the isoline plots. The asymmetric rotor was found to benefit from an increased saliency and reluctance torque (see Figure 19). Table 12 shows the flux density contour plots over the magnet regions during a short circuit. The blue regions show magnetization
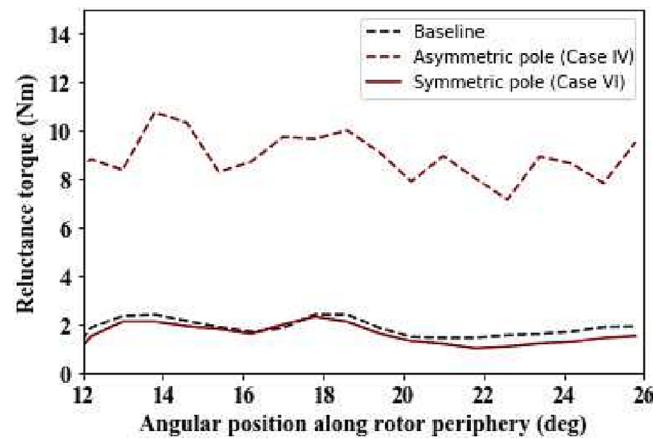
FIGURE 19   A comparison of reluctance torque predictions for optimized designs.

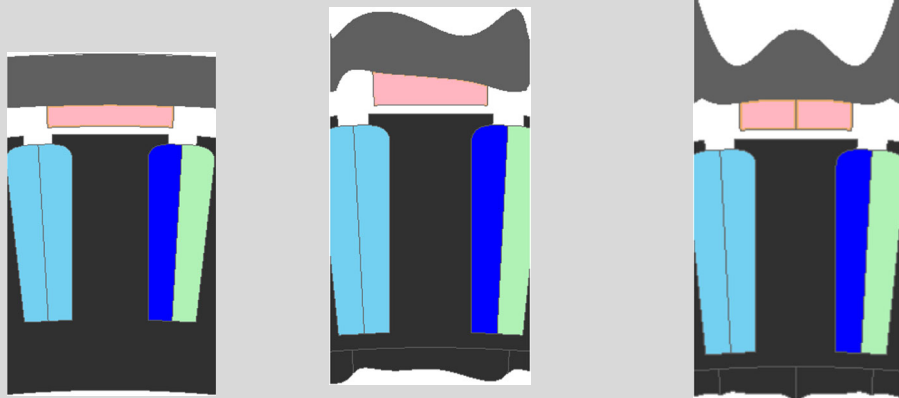**TABLE 12**   Flux density and temperature profiles in the magnets.

Optimized design	Asymmetric rotor and symmetric stator	Symmetric rotor and symmetric stator
Magnetic flux density profile		
Temperature profile		

lower than 0.5 Tesla with the lowest operating point constrained to be more than 0.3 Tesla. This outcome is also evident from the temperature distribution plots, which indicate no significant temperature rise in the magnets.

Results from a subsequent stator back-iron optimization using Cases IV and VI are shown in Table 13. For the asymmetric design, the material bias on the right-hand side of the back-iron region of the stator is notable. With a reduction in mass by up to 14.62 kg, the optimized designs were 20% lighter than the baseline stator.

Although these results are presented for a small direct-drive generator with outer rotor configuration and surface mounted magnets, the optimization method can be directly applied to multimegawatt wind turbine generators such as those studied in reference.[53] The inherent flexibility in parametrization of Bézier curves in cartesian and polar coordinates, together with a parametric CAD modeling tool, allows the curves to be readily usable in the optimization of other radial flux configurations with inner-rotor PMs, advanced magnet topologies such as Halbach arrays used in axial flux generators, and inset or interior permanent magnet machines used in larger machines[53] where additional parameters can be included.

TABLE 13 Results from optimization of the stator back iron.

Optimized design	Baseline design	Asymmetric rotor and stator back iron	Symmetric rotor and stator back iron
Rotor core mass (kg)	24.25	23.08	22.9
Magnet mass (kg)	7.31	5.37	5.99
Stator core mass (kg)	73.07	59.91	58.45
Efficiency (%)	96	96.89	96.99
T_{cog} (Nm)	27	23.18	24.28
ratio	71.62	60.64	60.2

TABLE 14 Regression analysis results and goodness of fit metrics.

Parameter	Coefficient	p-value	Fit
Multiple R	—	0.84	
$Adj - r^2$	—	—	0.68
Intercept	2994.92	9.59E-18	—
Front plate wall thickness	−2440.3	5.33E-19	—
Back plate wall thickness	−791.8	0.019	—
Radial wall thickness	−215.75	0.729	—
Fin height	−207.35	0.014	—
Fin thickness	830.4	0.21	—
Fin number	−6.84	0.62	–

5.2 | Structural evaluation

The regression analysis results are shown in Table 14. All treatment combinations satisfied the deformation constraints discussed in Section 4.2. The multiple R value of 0.84 suggests a relatively strong linear relationship between the six factors and the resultant stiffness-to-weight ratio. A goodness of fit of 0.68 with r^2 and adjusted-r^2 values (adj-r^2) is significant but not unusually strong. This adj-r^2 is likely caused by the number of factors that do not seem to significantly impact stiffness-to-weight. The p-values for each factor, shown in Table 14, indicate that the inside wall thickness, fin thickness, and fin number are not significant. Adding these factors to adj-r^2 would not improve the correlation. As a result, the factors with p-values less than 0.05 will not be included in the regression model.

Figure 20 shows the sensitivities of the stiffness-to-weight ratio to all the structural parameters of the rotor can. Most notable, the thickness of the radial wall had minimal effect on stiffness in the radial direction; however, this is also attributed to a small thickness of material (2.5 mm) between the chosen bounds. Because the radial wall is restricted by the magnetically optimized rotor profile, a nominal mass reduction was achievable by optimizing the thickness of the radial wall. Further, the asymmetric profile for the rotor can increase stiffness. Importantly, the wave-like profile creates axially oriented ridges that counteract the radial stress and limit deformation. In combination with the front bearing assembly, the radial wall does not see significant loading from the blades, meaning most of the radial stress and strain is caused by the magnetic forces.
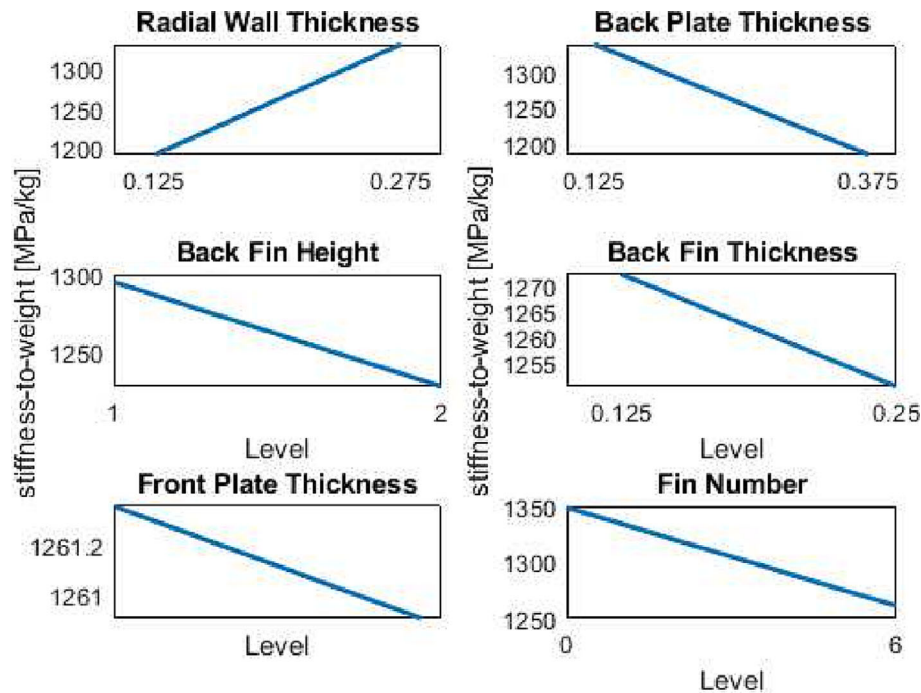
FIGURE 20   Main effects plot for each factor in the full-factorial design of experiment (FFDoE).

TABLE 15   Optimal solutions within the design space.

Parameter	Units	Baseline	Optimized	Realistic
Front plate thickness	mm	19.05	3.175	12.07
Back plate thickness	mm	9.525	3.175	3.175
Radial wall thickness	mm	10.312	3.175	3.175
Number of fins	—	0	0	0
Total structural mass	kg	108.83	77.4	95.16
Radial stiffness-to-weight	—	2028	1063.5	1617.2

Note: Baseline values are the originals, optimized values are from the regression analysis, and realistic values are the most practical values including manufacturing and maintenance concerns.

Considering that the number of fins is not significant, we decided to eliminate them. Note that the fin height factor has a *p*-value larger than 0.05, indicating that it is a significant factor. The taller fin will increase stiffness in the same way as a structural I-beam. Though this does increase stiffness, it also increases weight, and given that all treatments met the deformation requirements, the additional stiffness would not improve performance.

The significant factors included in the regression model are the front and back wall thicknesses. Although the number of fins is included as well, as discussed, they were not used. The linear regression model is given in Equation (11) where subscripts FW and BW refer to the front and back wall, and *int* is the intercept. The optimum factor combination is given in Table 15. Additionally, a second and more realistic set of parameters is provided based on discussions with our industry partners, which include assembly and maintenance concerns.

$$\frac{stiffness}{weight} = int + C_{FW} \cdot x_{FW} + C_{BW} \cdot x_{BW}. \tag{11}$$

We recognize that this second set of rotor can parameters is not a structurally optimal solution. The most obvious deviation from optimal is the front plate thickness, which is more than double what is necessary to support the blades and applied loads. The extra thickness is needed to create the proper thickness for the blade assembly hardware (i.e., the bolts holding the blades and reinforcement brackets to the generator). Further, this solution has not been designed for manufacture, cost minimization, or lifetime assessment analysis, so it is not known if this is an optimal

solution when considering other factors influencing the generator design and production. In terms of the rotor vibrational modes, the first and second harmonics of the rotor natural frequencies are not impacted significantly by this optimization because the extent of lightweighting was limited to less than 29% from the baseline (see Table 15). This was consistent with the observation made by the authors in Jaen-Sola et al.[54]

The support structure and stiffening features investigated in this work are applicable to can-like structures used in small direct-drive generators. The authors recognize that rotor support structures used in larger multimegawatt wind turbine generators utilize single-sided disk arrangements[53,55] with special housing. Implementing asymmetric poles on single-sided support structure will require a careful choice of design margins that consider contributions from from the magnets and any overturning moments that may potentially result in any eccentricity.

5.3 | Advanced manufacturing of optimized designs

The optimized magnet designs presented in this work can be produced by FDM 3D printing. ORNL's BAAM 3D printer has shown that it is possible to produce these magnets[20,22] because it can handle very high magnet filler loading. However, other commercially available printers may not be equipped to process the high-volume fraction material necessary for these magnets. An alternative approach would be to reduce the magnet loading volume by diluting the composite feed with a higher volume of polymer (50 vol% or less) or using an alternative additive manufacturing process such as injection molding.

In terms of the BAAM process described in references,[20,22] the feedstock is obtained by first pelletizing the composite magnet powder (Sm-Fe-N and Nd-Fe-B suspended in polymer binder) and then extruded through a heated nozzle that precisely deposits each layer onto a build platform. Each layer thickness corresponds to the extruder's nozzle diameter. To realize sharp curves and details in the wave patterns, printer tooling pathways need optimization. Other factors of the pellet extrusion system that need to be optimized are the screw rotation speed, melt zone temperature, and pellet feed rate for achieving consistent material flow and layer adhesion for wave-like patterns. The preforms of extruded magnets can be placed in a heated mold cavity of the final desired shape and subjected to high pressure, forcing the material to fill the mold completely and achieve high density by compression molding process as described in Vaidya et al.[56] During compression molding, 5%–7% porosity will be reduced. Following compression molding, the green (unmagnetized) magnet will require postannealing at temperatures up to 250°C under a magnetic field of 1–2 Tesla to orient the anisotropic particles and maximize magnetic remanence. Because it is a polymer bonded magnet, it can be attached directly to the printed rotor core by insert-molding through warm compaction.

The optimized rotor cores presented in this work can be manufactured by either SLM, indirect additive manufacturing, or wire EDM. SLM would require producing a rough printed part, which is then machined to the final dimensions. An alternative indirect additive manufacturing approach is to produce a sand mold with binder jetting and casting the rotor. This would potentially result in a rougher surface finish; however, this would not significantly impact performance.

In the case of optimized multimaterial magnet design (Case VII in Table 10), the two magnets can be manufactured by two independent methods, namely, sintering and FDM, and then stacked together with the help of a suitable adhesive. Another approach would be extrusion and compression molding of the printed magnet directly onto the layer of unmagnetized, sintered magnet. In this case, the binder of the printed polymer bonded magnet can serve as the adhesive. The composite multilayer magnet can then be attached to the rotor core as discussed previously.

The commercial approach to manufacturing near-net shaped stator lamination (as shown in Table 13) shall be by using high-precision laser cutting[9] and micromachining sheet laminations. Laser powder bed fusion methods such as SLM can also be used in achieving the near-net shape of the stator core followed by EDM slicing to the desired laminate thickness.

6 | CONCLUSIONS

This work demonstrated novel interpolar symmetric and asymmetric pole-shaping techniques for a surface mounted, outer rotor, radial flux DDPMSG by optimizing both hard and soft magnets at the same time. New, better-performing magnet and core designs were identified opening up a new design paradigm when designing wind turbine generators. We made several observations from the results, confirming previous hypotheses on symmetric designs and indicating that leveraging direction-dependence within the electromagnetic system can help tailor generator design for wind turbines by careful optimization. Although the results were discussed for small-scale direct-drive generators, the design methods introduced in this study can be readily scaled and applied for large-scale multimegawatt wind turbine generators, including those with different magnet topologies such as interior permanent machines, axial flux., and other advanced magnet geometries. With the help of advanced manufacturing techniques, the following beneficial performance effects can be realized:

- In terms of design exploration, asymmetry allows for more flexibility and new ways for material efficiency when compared to a symmetric approach to design. The magnet mass of the most optimal asymmetric design was 5.37 kg, which was 27% lighter when compared to the

baseline generator. This suggests a new opportunity to minimize the use of rare earth materials and to leverage advanced manufacturing processes for more compact and lightweight solutions without sacrificing performance.

- Although symmetrical designs often result in uniform magnetic fields within the machine, they can greatly limit the optimization of magnetic flux distribution and be too restrictive in terms of design space available for incorporating innovative features and materials, which could enhance their performance and efficiency. Results indicate that traditional symmetric design approach will necessitate the use of more magnet materials for a unidirectional application, such as in wind turbines, and result in a much larger or heavier machine than necessary. Yet, pole shaping can provide marginal improvements in performance.

- Interpolar asymmetric pole designs studied in this work have a recursive pattern. The magnet pressure distribution for asymmetric pole design represents that of a uniformly varying pressure load which is also periodic. This is generally consistent with the fact the magnet remanence behavior follows the thickness of magnet material along the pole pitch. Despite this variation, the peaks of the largest loads are still lower than the baseline design. Such asymmetric pole designs also benefit from a higher reluctance torque as a result of increased saliency.

- Detailed profiling of the air-gap side of the magnets (variable air-gap thickness) can improve cogging torque profile; but heavier magnet designs may result from a larger air gap for the same power output.

- Multilayered sintered and printed magnets have the highest potential to provide for magnet material savings with a mass of 4.77 kg which is 35% lighter when compared with the baseline design. Such configurations can be realized using advanced manufacturing techniques such as 3D printing that allow for multimaterial joining. Such layered configuration benefits from a higher coercivity of sintered magnets in air-gap region, which also lowers the risks from demagnetization.

- The undulating pattern on the rotor surface for asymmetric design can also serve as aerodynamic element that can be effective for better cooling of the generator.

- Shaping the stator back iron using symmetric and asymmetric poles helped reduce the electrical steel mass in the stator by 14.62 kg, which was 20% lighter than the baseline stator.

- Magnetically asymmetric rotor pole design was also shown to perform well structurally with a symmetric support structure design which suggested a new pathway for lightweighting wind turbine generators. Because the bearing system from the baseline generator was retained for the asymmetric rotor pole design and the magnitude of pressure peaks was significantly smaller than the baseline, and also periodic, the bearing loading is expected to be minimally impacted. Also, this pressure variation is expected to have little or no impact on the radial deformation of the rotor core where minimal material was removed. Further, the wave-shaped profile on the rotor cylinder creates axially oriented ridges that counteract the radial stress and limit deformation. The structural parametric analysis was able to produce an optimal solution within the design space, which reduced overall mass by approximately 30 kg. This is 29% lighter than the baseline. Radial stiffness decreased slightly, but all deformations remained within the desired range and the final solution is deemed acceptable.

- The structural design presented in this work may not be representative of larger multimegawatt wind turbine generators utilizing single-sided support structures. Such support structures, when used with asymmetric pole designs, would require a careful treatment of loads.

- The optimized pole designs presented in this work can be enabled by conducting FDM of magnets and insert- molding them onto the optimized rotor core, which can be manufactured by SLM or indirect additive manufacturing. High-power laser cutting as well as spark plasma sintering can also be used to enable such designs using sintered magnets. Multimaterial magnet designs can be realized by manufacturing the two magnets separately by sintering and FDM and then stacking them together with the help of a suitable adhesive.

- Commercially available laser powder bed fusion systems may have smaller build envelopes that limit the printability of full solid rotor core that was studied in this work. Indirect additive manufacturing using large sand molds shows more promise for casting metal, such as ductile-iron for such dimensions. It is also possible to print the stator laminations of dimensions studied in this work by using the laser powder bed approach where opportunities to integrate insulation layers with laminates are possible by using multimaterial printing.

Future work is planned to advance optimization methods for shape-profiled windings, develop printing cost models, and perform a gap analysis for manufacturing large-scale wind turbine generators. Additional activities include validating the methods and designs through a prototype demonstration of a 15-kW generator to de-risk and transform the technology to robust and scalable solution through follow-on funding.

ORCID

Latha Sethuraman https://orcid.org/0000-0001-6270-0430

REFERENCES

1. Jenkins J, Forsyth T, Summerville B, others. Smart wind roadmap: a consensus-based,shared-vision sustainable manufacturing,advanced research & technology action plan for distributed wind. tech. rep., Distributed Wind Energy Association; 2016. Available at: https://distributedwind.org/wp-content/uploads/2016/05/SMART-Wind-Roadmap.pdf

2. Mordor Intelligence. Small wind turbine market size & share analysis - growth trends & forecasts (2024 - 2029). tech. rep.; 2023. Available at: https://www.mordorintelligence.com/industry-reports/small-wind-turbine-market

3. Bianchini A, Galih B, Bangga GI, et al. Current status and grand challenges for small wind turbine technology. *Wind Energy Sci*. 2022;7(5):2003-2037.

4. Smith BJ, Riddle ME, Earlam MR, Iloeje C, Diamond D. Rare earth permanent magnets: supply chain deep dive assessment. tech. rep., U.S. DOE Office of Policy (PO); 2022. https://doi.org/10.2172/1871577

5. Drives & Controls. Soaring steel costs are hitting motor prices and lead times. Available at: https://drivesncontrols.com/news/fullstory.php/aid/7094/Soaring_steel_costs_are_hitting_motor_prices_and_lead_times.html, Accessed August 29, 2023; 2022.

6. Development of a concentrated winding PM alternator for a small wind turbine. Tech. Rep. SBIR Report, Bergey; 2021.

7. Muljadi E, Green J. Cogging torque reduction in a permanent magnet wind turbine generator. In: 21st American Society of Mechanical Engineers Wind Energy Symposium; 2002. https://doi.org/10.2514/6.2002-56

8. Fraunhofer IFAM. EffiBlech: project for efficient and resource-saving engine production started: Fraunhofer ifam dresden develops printed metal sheets for electric drives. Available at: https://www.ifam.fraunhofer.de/content/dam/ifam/en/documents/dd/PressReleases/FraunhoferIFAMDresdendevelopsprintedmetalsheetsforelectricdrives.pdf, Accessed August 29, 2023; 2021.

9. Hi-tech laser cutting for electric motors development: Aussafer due. Available at: https://www.electricmotorengineering.com/hi-tech-laser-cutting-for-electric-motors-development-aussafer-due/, Accessed September 2, 2023.

10. Edgar-Lane C. Motor lamination manufacturing processes: a comparison of stamping, laser cutting and chemical etching. Available at: https://www.precisionmicro.com/motor-lamination-manufacturing-processes-a-comparison-of-stamping-laser-cutting-and-chemical-etching/, Accessed September 3, 2023.

11. KDMFAB. Hydroforming process—the ultimate guide. Available at: https://kdmfab.com/hydroforming-process/, Accessed Septemebr 2, 2023.

12. Cramer CL, Nandwana P, Yan J, et al. Binder jet additive manufacturing method to fabricate near net shape crack-free highly dense fe-6.5 wt.% si soft magnets. *Heliyon*. 2019;5(11):e02804.

13. Lamichhane TN, Wang H, Chinnasamy C, et al. Additively manufactured Fe-3Si stator for a high-performance electrical motor. Available at SSRN: https://doi.org/10.2139/ssrn.4086824

14. Wang H. Additive manufacturing of magnetic materials for electric motor and generator applications. *PhD Thesis*: The University of Tennessee, Knoxville; 2023.

15. GE. GE renewable energy, Fraunhofer IGCV, and voxeljet AG plan to develop world's largest sand binder jetting 3D printer for offshore wind turbines. Available at: https://www.ge.com/news/press-releases/ge-renewable-energy-fraunhofer-igcv-voxeljet-plan-develop-world-largest-sand-binder-jetting-3D-printer-offshore-wind-turbines, Accessed September 2, 2023.

16. Sand 3D printers. Available at: https://exone.com, Accessed August 29, 2023.

17. Tomše T, Samardžija Z, Scherf L, et al. A spark-plasma-sintering approach to the manufacture of anisotropic Nd-Fe-B permanent magnets. *J Magnet Magnet Mater*. 2020;502:166504.

18. Cui J, Ormerod J, Parker DS, et al. Manufacturing processes for permanent magnets: part II-bonding and emerging methods. *J Mater*. 2022;74:2492-2506.

19. Aichi Steel Corporation. Magfine® technical datasheet. Available at: https://www.aichi-steel.co.jp/_assets/pdf/products/smart_company/magfine/magfine_datasheet.pdf, Accessed August 29, 2023; 2018.

20. Liu XB, Gandha K, Wang H, et al. Packing bimodal magnetic particles to fabricate highly dense anisotropic rare earth bonded permanent magnets. *RSC Adv*. 2023;13(25):17097-17101.

21. Labuschagne CJJ, Sethuraman L, Hanley T, et al. An assessment of additively manufactured bonded permanent magnets for a distributed wind generator. In: 2023 IEEE International Electric Machines & Drives Conference (IEMDC); 2023:1-7. NREL/CP-5000-85626. https://www.nrel.gov/docs/fy23osti/85626.pdf

22. Gandha K, Paranthaman MP, Wang H, et al. Thermal stability of anisotropic bonded magnets prepared by additive manufacturing. *J Am Ceram Soc*. 2023;106:166-171.

23. Kemp JW, Mungale K, Wang H, et al. Novel method for overmolding of NdFeB bonded magnets into a 3D printed rotor. *IEEE Trans Magnet*. 2023.

24. Sethuraman L, Vijayakumar G, Ananthan S, et al. MADE3D: enabling the next generation of high-torque density wind generators by additive design and 3D printing. *Forsch Ingenieurwes*. 2021;85:287-311.

25. McGarry C, McDonald A, Alotaibi N. Optimisation of additively manufactured permanent magnets for wind turbine generators 2019 IEEE International Electric Machines & Drives Conference (IEMDC); 2019:656-663. https://doi.org/10.1109/IEMDC.2019.8785119

26. Tian J, Zhuang R, Cilia J, et al. Topology optimization of permanent magnets for generators using level set methods. In: International design engineering technical conferences and computers and information in engineering conference, Vol. 86236 American Society of Mechanical Engineers; 2022: V03BT03A037. https://doi.org/10.1115/DETC2022-90601

27. Lee JH, Kim DH, Park IH. Minimization of higher back-EMF harmonics in permanent magnet motor using shape design sensitivity with b-spline parameterization. *IEEE Trans Magnet*. 2003;39(3):1269-1272.

28. Faezian G, Darabi A, Sargolzaei N. Customized shape optimization of switched reluctance motor using b-splines. *COMPEL*. 2021;40(3):402-413.

29. Sethuraman L, Vijayakumar G. A new shape optimization approach for lightweighting electric machines inspired by additive manufacturing. In: 2022 Joint MMM-INTERMAG Conference; 2022:1-7. https://doi.org/10.1109/INTERMAG39746.2022.9827714

30. Liu C, Xu Y, Zou J, et al. Permanent magnet shape optimization method for PMSM air gap flux density harmonics reduction. *CES Trans Electr Machines Syst*. 2021;5(4):284-290.

31. Wang K, Gu ZY, Zhu ZQ, Wu ZZ. Optimum injected harmonics into magnet shape in multiphase surface-mounted PM machine for maximum output torque. *IEEE Trans Industr Electron*. 2017;64:4434-4443.

32. Zentao SD, Lipo TA. High torque density and low torque ripple shaped-magnet machines using sinusoidal plus third harmonic shaped magnets. *IEEE Trans Indust Appl*. 2019;55(3):2601-2610.

33. Sun X, Sizov G, Melfi M. Asymmetrical design in electric machines. In: 2019 IEEE Energy Conversion Congress and Exposition (ECCE); 2019:3786-3792. https://doi.org/10.1109/ECCE.2019.8913231

34. Devito G, Nuzzo S, Barater D, Soltani M, Franceschini G. Combined magnet shaping and asymmetries in surface-mounted permanent magnet machines for improved torque performance. In: 2022 International Conference on Electrical Machines (ICEM); 2022:855-861. https://doi.org/10.1109/ICEM51905.2022.9910726

35. Mirahki H, Moallem M, Ebrahimi M, Fahimi B. Asymmetrical magnet shape optimization based on S-C mapping for torque profile mitigation in unidirectional application of SPMS machine. *IEEE Trans Transport Electrific*. 2019;5(3):630-637.

36. Naseer MU, Kallaste A, Asad B, Vaimann T, Rassõlkin A. A review on additive manufacturing possibilities for electrical machines. *Energies*. 2021;14: 1940.

37. Yang N, Cao W, Liu Z, et al. Novel asymmetrical rotor design for easy assembly and repair of rotor windings in synchronous generators. In: 2015 IEEE International Magnetics Conference (INTERMAG); 2015:1. https://doi.org/10.1109/INTMAG.2015.7156694

38. Zahangir T. Analysis of asymmetrical features of an electric machine. *M.S. Thesis*: Chalmers University of Technology, Sweden; 2018.

39. Petrov I, Ponomarev P, Pyrhönen J. Asymmetrical geometries in electrical machines. *Int Rev Electr Eng*. 2016;11(1):20. https://doi.org/10.15866/iree.v11i1.7739

40. Farshbaf F. Asymmetric design: a way for optimizing electric motor's performance. https://www.emworks.com/blog/motor-design/asymmetric-design-a-way-for-optimizing-electric-motors-performance, Accessed August 29, 2023; 2022.

41. Sethuraman L, Glaws G, Skinner M, Paranthaman MP. Advanced permanent magnet generator topologies using multimaterial shape optimization and 3d printing. In: 12th International Conference on Power Electronics, Machines and Drives (PEMD 2023); Brussels, Belgium, 2023:475-485. https://doi.org/10.1049/icp.2023.2041

42. Altair-Flux®. Available at: https://www.altair.com/flux-applications/, Accessed June 20, 2023.

43. Paviot T. Pythonocc (7.7.2) Edited by Zenodo. Available at: https://www.github.com/tpaviot/pythonocc-core

44. Santner TJ, Williams BJ, Notz WI, Williams BJ. *The design and analysis of computer experiments*, Vol. 1: Springer; 2003.

45. Sjögren R, Svensson D. pyDOE2: an experimental design package for python: Clicumu. Available at: https://www.github.com/clicumu/pyDOE2; 2018.

46. OpenCASCADE technology. 7.5.1 library. Available at: https://dev.opencascade.org/, Accessed August 29, 2023.

47. Dassault Systèmes. Solidworks®. Version 2022.

48. Sacks J, Welch WJ, Mitchell TJ, Wynn HP. Design and analysis of computer experiments. *Stat Sci*. 1989;4(4):409-423. https://doi.org/10.1214/ss/1177012413

49. Constantine PG. *Active subspaces: Emerging ideas for dimension reduction in parameter studies*: SIAM; 2015.

50. Glaws A, Constantine PG, Cook RD. Inverse regression for ridge recovery: A data-driven approach for parameter reduction in computer experiments. *Stat Comput*. 2020;30:237-253.

51. Hokanson JM, Constantine PG. Data-driven polynomial ridge approximation using variable projection. *SIAM J Scientif Comput*. 2018;40(3):A1566-A1589.

52. Constantine PG, Eftekhari A, Hokanson J, Ward RA. A near-stationary subspace for ridge approximation. *Comput Methods Appl Mech Eng*. 2017;326: 402-421.

53. Barter GE, Sethuraman L, Bortolotti P, Keller J, Torrey DA. Beyond 15 mw: A cost of energy perspective on the next generation of drivetrain technologies for offshore wind turbines. *Appl Energy*. 2023;344:121272.

54. Jaen-Sola P, McDonald AS, Oterkus E. Dynamic structural design of offshore direct-drive wind turbine electrical generators. *Ocean Eng*. 2018;161: 1-19.

55. Gaertner E, Rinker J, Sethuraman L, et al. Definition of the iea 15-megawatt offshore reference wind. tech. rep., National Renewable Energy Laboratory; 2020. Available at: https://www.nrel.gov/docs/fy20osti/75698.pdf

56. Vaidya UK, Paranthaman MP, Kunc V, Hassen AA. Extrusion-compression method for producing bonded permanent magnets. U.S. Patent Application No. 17/529,588; 2022.